Article

Exploring Wave–Vegetation Interaction at Stem Scale: Analysis of the Coupled Flow–Structure Interactions Using the SPH-Based DualSPHysics Code and the FEA Module of Chrono

Joe El Rahi [1,*], Iván Martínez-Estévez [2], Rui Almeida Reis [3], Bonaventura Tagliafierro [4,5], José M. Domínguez [2], Alejandro J. C. Crespo [2], Vasiliki Stratigaki [1], Tomohiro Suzuki [6,7] and Peter Troch [1]

[1] Department of Civil Engineering, Ghent University, Technologiepark 60, 9052 Ghent, Belgium
[2] Environmental Physics Laboratory, Centro de Investigación Mariña (CIM-UVIGO), Universidade de Vigo, Campus As Lagoas, 32004 Ourense, Spain
[3] Hydraulics and Environment Department, National Laboratory for Civil Engineering (LNEC), Avenida do Brasil 101, 1700-066 Lisbon, Portugal
[4] Department of Civil and Environmental Engineering (DECA), Universitat Politecnica de Catalunya, Jordi Girona, 08034 Barcelona, Spain
[5] School of Natural and Built Environment, Queen's University Belfast, Belfast BT9 5AG, UK
[6] Flanders Hydraulics, Berchemlei 115, 2140 Antwerp, Belgium
[7] Department of Civil Engineering, KU Leuven, Kasteelpark Arenberg 40, 3001 Leuven, Belgium
* Correspondence: joe.elrahi@ugent.be; Tel.: +32-9-264-54-89

Abstract: Aquatic vegetation in the littoral zone plays a crucial role in attenuating wave energy and protecting coastal communities from hazardous events. This study contributes to the development of numerical models aimed at designing nature-based coastal defense systems. Specifically, a novel numerical application for simulating wave–vegetation interactions at the stem scale is presented. The numerical model employed, DualSPHysics, couples the meshfree Smoothed Particle Hydrodynamics (SPH) fluid solver with a structural solver to accurately capture the two-way interactions between waves and flexible vegetation. The proposed numerical model is validated against experimental data involving a submerged rubber cylinder representing an individual vegetation stem, subjected to regular waves. The results demonstrate excellent agreement in hydrodynamics, force transfer, and the swaying motion of the flexible cylinder. Importantly, the approach explicitly captures energy transfer between the fluid environment and the individual stem. The numerical results indicate persistent turbulent flow along the vegetation stem, even when its swaying speed matches that of the surrounding environment. This reveals the presence of vortex shedding and energy dissipation, which challenges the concept of passive swaying in flexible aquatic vegetation.

Keywords: wave–vegetation interaction; flexible structure; fluid–elastic structure interaction; SPH-FEA coupling; DualSPHysics; Project Chrono

1. Introduction

Aquatic vegetation in marine environments, such as seagrass, is gaining recognition for the positive net effect it has on the hosting ecosystem [1–3]. Firstly, it mitigates coastal hazards by absorbing wave energy and reducing water flow velocity [4–7]. Secondly, it plays a role in regulating nutrient levels, provides food-rich habitats for marine species, and contributes to the absorption of carbon dioxide [8–10]. Thirdly, it functions as a dynamic, nature-driven adaptation mechanism on multiple fronts. Below the seabed, its root systems and rhizomes reduce erosion; and within the water column, the turbulent flows within the canopies facilitate sediment deposition and promote accretion [11,12].

From the standpoint of urban planners and coastal engineers, a pivotal concern revolves around safeguarding coastal communities against the escalating coastal hazards, all while maintaining a minimal carbon footprint [13,14]. Consequently, there is

a growing emphasis on the integration of nature-based defense solutions, such as seagrasses, within coastal planning strategies [15]. An effective approach to quantify the influence of seagrasses on the coastal wave dynamics is the utilization of advanced numerical techniques.

Numerical models are capable of simulating wave–vegetation interactions across a range of scales. For example, spectral models, such as SWAN [16], are capable of simulating climate scenarios and forecasting wave parameters over extensive domains and extended time periods [17,18]. At a smaller scale, phase-resolving models, such as the non-hydrostatic model SWASH [19], can provide wave forecasts in (relatively) shallow environments, covering domains spanning multiple kilometers (at the study area level) over extended periods (e.g., wave transformation over coastal vegetation in the South China Sea [20]). In contrast, more intricate Computational Fluid Dynamics (CFD) models, which resolve the Navier–Stokes (NS) equations by discretizing the computational domain into a large number of nodes, are better suited for short durations in smaller domains spanning over a distance of a few wavelengths. For example, Marjoribanks et al. [21] employed a model based on finite volume and the large eddy simulation (LES) to simulate canopy flow and turbulence dynamics in an open-channel flow. A similar approach was used by Wang et al. [22] to assess the drag exerted by a rigid and flexible vegetation stem. In a separate study addressing coastal hydrodynamics, Maza et al. [23] employed a CFD model to simulate wave attenuation through a drag term that accounts for vegetation flexibility.

Zeller et al. [24] classified the numerical models operating at various scales into three categories:

- Category 1, stem or canopy scale;
- Category 2, meadow scale;
- Category 3, ecosystem or coastal-scale ocean models.

At each scale, specific modeling techniques are employed in order to address the influence of vegetation. At the stem or canopy scale (Category 1), a direct approach is applicable. In a direct approach, the interaction between the fluid and the structure is explicitly solved by representing the vegetation as a flexible boundary element within the fluid domain and numerically solving the force transfer and vortex shedding around the vegetation. This is achieved by resolving the physics with a high-fidelity model without assumptions or simplifications on the geometry (i.e., computationally expensive techniques are limited to small domains, for example [25]).

At larger scales such as meadow and ecosystem scales, ocean models utilize the computationally efficient drag force [26,27] and bed roughness approaches [28]. Figure 1 illustrates the three numerical techniques in an artistic representation. The direct approach preserves the physical attributes of the vegetation patch, whereas the cylinder approach simplifies it into an array of cylinders. Finally, the bed roughness approach incorporates vegetation numerically by introducing a dissipative term at the seafloor, as indicated by the black region in the top right panel of Figure 1. The mechanism underlying vegetation-induced wave attenuation is consistent across all three scales and can be described as the dissipation of wave energy due to the resistance that vegetation imposes on the flow. This can be estimated by multiplying the relative velocity between the fluid and vegetation by the normal force component and integrating it over the surface area. In order to provide an accurate description of this attenuation formulation, it is necessary to consider the effect of vegetation flexibility on the relative velocity between the fluid and the vegetation. A greater degree of flexibility will result in a reduction in the relative velocity between the fluid and the vegetation, which will consequently lead to a reduction in the energy attenuation.
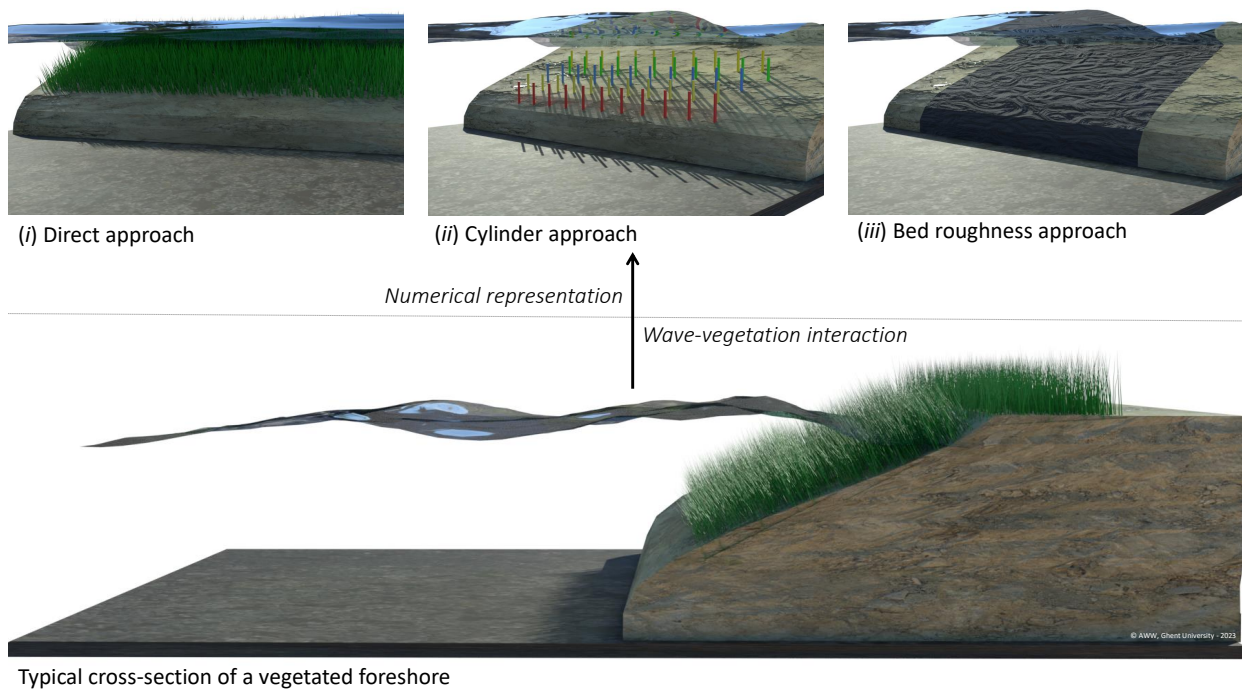
(*i*) Direct approach (*ii*) Cylinder approach (*iii*) Bed roughness approach

Numerical representation

Wave-vegetation interaction

Typical cross-section of a vegetated foreshore

Figure 1. Artistic representation of the wave–vegetation interaction process within the coastal zone: the lower panel displays a typical foreshore cross-section, illustrating waves interacting with vegetation on a vegetated slope; and the upper panel displays three numerical techniques for simulating the wave–vegetation interaction and subsequent energy dissipation, namely: (**i**) the direct approach, (**ii**) the cylinder approach, and (**iii**) the bed roughness approach.

The present study focuses on resolving wave–vegetation interaction at the stem scale, specifically, within the domain of "Category 1, stem or canopy scale". In this category, the research objective is to develop numerical modeling techniques for resolving one or multiple dimensions of the wave–vegetation interaction. These dimensions include:

1. The swaying motion of individual flexible elements;
2. The flow properties;
3. Energy transfer mechanisms.

A well-established approach for addressing the swaying motion is to model vegetation flexibility using a cantilever beam element and solve deflections using the Euler–Bernoulli formulation (e.g., [29–31]). The flexural rigidity of the vegetation, defined as the resistance to bending, is replicated numerically by defining the section properties of the beam and Young's modulus of elasticity (E). Numerous studies have successfully simulated stem dynamics by employing a standalone structural model and computing the force balance on the vegetation by fitting a velocity curve to data obtained from laboratory experiments [24,32–34]. This is typically achieved by applying the Morison equation [35] to calculate drag, inertia, lift, and skin friction forces. In order to account for the other forces present in the system, it is necessary to include buoyancy, gravity, added mass, and hydrostatic forces.

Building upon the previously described method, coupled models have been developed to explore multiple dimensions of wave–vegetation interaction at the stem scale. These coupled models combine flow solvers with structural solvers in order to accurately replicate the flow field around the vegetation. For instance, in the study conducted by Yin et al. [36], the XBeach non-hydrostatic model [37] was employed to communicate both: (i) the depth-averaged velocity in one direction (from fluid to structure and not the other way around), and (ii) the time-varying force on a flexible element in the other. The subsequent consideration of the impact of these inputs on the wave propagation involved

the introduction of a dissipation term into the momentum equation. A similar approach using SWASH was presented in [38].

El Rahi et al. [39] employed the meshless Smoothed Particle Hydrodynamics-based (SPH) [40] code, DualSPHysics [41], to investigate flow dynamics while also proposing a coupled approach [42] to tackle vegetation dynamics. The method's applicability can vary depending on the specific case since it relies on an embedded approach to represent vegetation within a larger dummy boundary envelope. This approach is particularly well-suited for specific scenarios in which buoyancy-restoring forces have a limited impact, and the vegetation assumes a rectangular cross-section (limitation to one geometric shape) with minimal thickness relative to the wavelength of periodic water waves. In a separate study employing the SPH method, Paquier et al. [43] simulated flexible vegetation using the slender rod theory. Within this numerical model, adjustments were made to increase the dimensions of the vegetation and simultaneously modify the section properties to ensure that the same deflection observed in the experiments was reproduced. While the previously mentioned models have simplified certain aspects of the real system, a direct computation of the kinetic energy is necessary to comprehensively account for all dimensions within the system. This can be achieved through the utilization of small-scale numerical models as shown in [25,44].

This study addresses the limitations in previous numerical models suited for wave–vegetation interactions. The proposed numerical approach offers a novel contribution by directly capturing all three dimensions of the wave–vegetation interaction: the swaying motion, the flow properties, and the energy transfer. Additionally, it captures the vortex shedding phenomena around the flexible cylinder. The coupled model combines DualSPHysics with the Finite Element Analysis (FEA) module of Project Chrono and is based on the implementation presented in [42]. To ensure accuracy, a numerical framework is established for configuring and validating both the structural and fluid solvers based on well-established analytical solutions. This framework creates a pathway for potential future studies exploring wave–vegetation interactions at stem or canopy scales.

This paper presents an experimental dataset obtained from the laboratory tests of Reis et al. [45]. The dataset involves a flexible cylinder, representing an individual vegetation stem, subjected to regular water waves. This dataset serves as a validation dataset for the numerical model, enabling an examination of the wave–vegetation interactions at stem scale. The numerical methods are detailed in Section 2, followed by the presentation of the physical laboratory tests in Section 3 and numerical framework in Section 4. The results are showcased in Section 5 and discussed in Section 6, with conclusions drawn in Section 7.

2. Numerical Methods

The direct numerical model employed in this study comprises three components: a fluid solver (DualSPHysics), a structural solver (FEA of CHRONO), and a two-way coupling interface. The following sections provide a detailed description of each component and present the corresponding governing equations.

2.1. SPH Method

The open-source software DualSPHysics (https://dual.sphysics.org/) [41], which is based on the SPH method and released under the GNU Lesser General Public License (LGPL), is used in this study. DualSPHysics is well-suited for wave generation and propagation in numerical flumes. It incorporates a set of boundary conditions, wave generation methods, and absorption techniques. The stability it exhibits also makes it particularly suitable for engineering studies where results can be compared to experimental datasets. Moreover, it has demonstrated efficacy as an engineering tool for investigating wave–vegetation interaction [39]. DualSPHysic's architecture is expandable and allows communication with other solvers. It has been coupled with Chrono [46] to address complex mechanical systems and multi-body conditions [47], including the incorporation of flexible elements through the FEA library [42].

The SPH method employs spatial discretization with particles to divide the domain into a finite number of data points where physical quantities are defined. The dynamics of each particle is then computed based on the attributes of neighboring particles that fall within a distance controlled through a distance function. To solve the motion of the particles, the neighbor list and physical quantities such as velocity, pressure, position, and density are calculated at each time step.

In fluid mechanics, the NS equations can be reordered to become suitable for the SPH method using a continuous integral function, termed kernel, W. The resulting governing momentum Equation (1) and continuity Equation (2) equations are:

$$\frac{d\mathbf{v}_a}{dt} = -\sum_b m_b \left(\frac{P_a + P_b}{\rho_a \rho_b} + \Gamma \right) \nabla_a W_{ab} + \mathbf{g} \tag{1}$$

$$\frac{d\rho_a}{dt} = \rho_a \sum_b \frac{m_b}{\rho_b} \mathbf{v}_{ab} \nabla_a W_{ab} + 2\delta h c \sum_b (\rho_a - \rho_b) \frac{\mathbf{v}_{ab} \nabla_a W_{ab}}{\mathbf{r}_{ab}^2} \frac{m_b}{\rho_b} \tag{2}$$

with a and b being two distinct particles representing the fluid, and where t, $\mathbf{v}$, P, and $\mathbf{g}$ are the time, velocity, pressure, and gravitational acceleration, respectively. The gradient operator is represented using ∇_a, and the kernel function W_{ab} [48]. The dissipative term Γ in the momentum equation is solved using the laminar viscosity model [49] and Sub-Particle Scale (SPS) turbulence model [50,51]. Finally, $\mathbf{r}_{ab}^2$ is the distance between particles a and b, c is the speed of sound, and δ is a diffusion parameter.

The Weakly Compressible form of SPH (WCSPH) [52] is used in DualSPHysics. This formulation creates a coupled environment that connects density and pressure using Tait's equation of state [53]. The fluid pressure, P, is calculated according to the following equation that accommodates minor density fluctuations:

$$P = \frac{c^2 \rho_0}{\gamma} \left[\left(\frac{\rho}{\rho_0} \right)^\gamma - 1 \right] \tag{3}$$

with the fluid density (1000 kgm^{-3} for water) being ρ_0, γ being the polytechnic constant, and c the speed of sound. Since this formulation might encourage non-physical fluctuations in the density field, DualSPHysics also includes a density diffusion term that acts as a low-pass filter for the numerical noise present in the system.

2.2. Structural Solver

The non-linear FEA module from Chrono is employed to simulate flexible structures using the Euler–Bernoulli beam. This element is capable of handling structural deformation and is suitable for simulating any type of structural scheme, including cantilevered configurations that are relevant to applications involving flexible vegetation. Further details on the implementation of the Euler–Bernoulli beam element can be found in the work of Tasora et al. [46].

The Euler–Bernoulli corotational beam theory enables the consideration of large deflections while maintaining a restriction to small strains. In the structural solver, the beam is parameterized by the user-defined geometrical parameters, including the area moments of inertia (I_{zz} and I_{yy}) along the z-axis and y-axis, respectively, the cross-sectional area (A), and the length (L). Additionally, the material properties, Young's modulus E, Poisson's ratio ν_v, and density ρ_v, must be specified. Moreover, the incorporation of mass and stiffness proportional damping, regulated by an input coefficient, c_s, is possible. Note that through the utilization of small damping coefficients, this damping mechanism could be employed to improve the stability of the numerical scheme.

The deflection, denoted as $\phi(x)$, along the length x of a beam subjected to a transverse load $q(x)$, is calculated using the following formula:

$$q(x) = \frac{d^2}{dx^2} EI \left(\frac{d^2 \phi(x)}{dx^2} \right) \tag{4}$$

The displacements and rotations of the beam element are determined at localized positions along the beam, which are referred to as nodes. These nodes are ordered along the center line of the beam, with each pair connected by a segment. The number of segments, designated as N, determines the resolution of the beam element.

2.3. Two-Way Coupling

Communication between the fluid and the structural solver is achieved through the incorporation of the beam into the SPH domain, utilizing a set of boundary particles that represent the beam element's geometry [42]. To distinguish them in SPH terminology, these particles are referred to as beam particles. The initial inter-particle distance (dp) remains consistent for all particles within the SPH domain, including fluid, boundary, and beam particles. In order to account for the potential impact of buoyancy forces on the dynamics of the wave–vegetation problem, the beam particles in SPH are part of the same floating body and include the definition of the density attribute.

The interaction between the fluid and the structure is resolved by computing the total force exchange. The geometry of the structure is represented in the SPH domain using boundary particles denoted by K. For each boundary particle $a \in K$, the velocity is calculated based on the fluid particles $b \in F$ following Equation (5).

$$\frac{d\mathbf{v}}{dt}\bigg|_{a \in K} = \sum_{b \in F} m_b \frac{d\mathbf{v}_{ab}}{dt} \tag{5}$$

Following that, the force vector $\mathbf{F}$ acting on the structure can be obtained following Equation (6):

$$\mathbf{F} = \sum_{a \in K} m_a \frac{d\mathbf{v}_a}{dt} \tag{6}$$

The interaction is solved across the complete boundary interface in 3D. Consequently, both pressure and shear stresses are considered when computing the force. Furthermore, the turbulence closure model (laminar viscosity + SPS Turbulence) present in the momentum equation (Equation (1)) is solved to calculate the velocities at the boundary. This ensures that the effects of flow separation and vortex shedding within the boundary layer are accounted for in the force computation.

During each SPH timestep, denoted as Δt_{SPH}, the forces experienced by the beam particles are assigned to the corresponding segments and transmitted to the structural solver (Chrono). An independent structural timestep, denoted as Δt_{CH}, is employed for the purpose of addressing structural deformation. Multiple iterations may occur until $\sum \Delta t_{CH} >= \Delta t_{SPH}$. Once equality is reached, the updated node positions (reflecting the deformed shape) are communicated with DualSPHysics. Subsequently, the positions of the beam particles are adjusted to represent the deflected shape. For a comprehensive understanding of this coupling methodology and presentation of benchmark validation cases, refer to [42].

3. Experimental Data

In order to validate the numerical model, the laboratory data presented by Reis et al. [45] are employed. This section provides a comprehensive overview of the experimental setup, hydraulic conditions, and methodology employed.

Wave flume laboratory testing was conducted at the National Laboratory for Civil Engineering (LNEC) in Lisbon, Portugal. The wave flume has a length of 33 m and is equipped with a piston-type wave generator and a sloped beach absorber. A 1/20 (one-in-twenty) concrete slope was constructed 12 m away from the wave paddle, leading to a 7.12 m long false bottom. On top of the false bottom, a 5 m long artificial vegetation patch was created using cylindrical elements that imitate natural vegetation. Two types of artificial vegetation fields were tested during the experimental campaign. These fields were constructed using either rigid pine wood cylinders or flexible sponged rubber cylinders. Both cylinder configurations featured identical geometrical dimensions: a diameter, D,

of 0.01 m and a total length, *L*, of 0.25 m in a neutral vertical posture. The tests had a total duration of 200 s. In-phase synchronized measurements were conducted for various parameters, including: (i) free surface elevation, η, measured using a resistive-type wave gauge, (ii) horizontal water velocity, *u*, determined with a Nortek Vectrino acoustic Doppler velocimeter, and (iii) horizontal force component, F_x, on an individual element, measured using a force transducer. The forces were recorded using a load cell with a linear voltage output and operating range from −1.5 N to 1.5 N. To avoid flow disturbance, the load cell, connected to the bottom of the flexible cylinder, was embedded into a hollow PVC box situated below the false bottom. Furthermore, data of the flexible vegetation motion and of free surface elevation were obtained from video analysis synchronized with the instrumental measurements. Further details of the experimental setup, wave dissipation results, vegetation motion analysis, and drag coefficients are published in Reis et al. [45].

The objective of the present study is to investigate interactions at the stem scale. Therefore, the array of cylinders in the wave flume is disregarded, and only a single flexible cylinder positioned at the center of the patch is examined. The experiment's measurement setup is tailored to capture the surrounding forcing environment around this central cylinder with high resolution. Moreover, the arrangement of the array ensures sufficient spacing between the upstream and downstream cylinders to minimize interference.

A single experiment was selected to configure and validate the numerical model. In this experiment, the forcing environment was recorded using: (i) a resistive wave gauge to measure surface elevation at the cylinder's location and (ii) a Vectrino to measure horizontal water velocity at *z* = 0.175 m (reference level being the bottom of the flume), which is approximately half the water depth, and (iii) a force transducer to measure the horizontal force component, F_x, applied on the flexible cylinder. The swaying characteristics of the flexible cylinder, including the swaying distance and speed, were determined through video tracking analysis applied to the video recording. Further details on the wave conditions and cylinder characteristics of the selected experiment can be found in Table 1.

Table 1. Physical parameters of the selected experimental test.

Hydrodynamic Conditions	
Test ID	Sr07_T14_H09
Wave type	Regular
Wave height, *H* [m]	0.09
Wave period, *T* [s]	1.40
Water depth, *h* [m]	0.35
Wavelength, λ [m]	2.28
Flexible Cylinder Characteristics	
Geometry	Cylinder
Material	Sponged rubber
Length, *L* [m]	0.25
Diameter, *D* [m]	0.01
Young's modulus, *E* [MPa]	0.82
Density, ρ_v [kgm^{-3}]	290

4. Numerical Framework

The numerical model is configured to replicate the experimental conditions described in Section 3. The two-way SPH-FEA coupling within DualSPHysics is employed as a unified platform to resolve the wave propagation, force transfer, and structural deflections.

The dimensions and parameters of the flexible cylinder, as reported in the experimental study, are used in the numerical model without any scaling. This approach renders the simulation of thin and highly flexible elements in hydrodynamic environments computationally expensive. As an illustration, consider the extreme case presented in the setup of Luhar and Nepf [33], where a blade with a thickness of 0.0004 m is used. On the other side of the spectrum, the experimental setup presented above includes a cylinder with a

diameter of 0.01 m. In any case, this ratio between the resolution required to resolve the fluid dynamics and the resolution required to discretize the structure tends to be large. Given that DualSPHysics only supports a uniform resolution, a substantial number of computational nodes is required. Moreover, when addressing wave–vegetation interactions, it is crucial to account for drag and inertia, flow streamlines extending across the width of the vegetation, and pressure gradients between the upstream and downstream sides. This can exclusively be simulated in a 3-D environment.

Considering these factors is crucial when creating a numerical environment based on laboratory experiments. In the present study, two adjustments are made in configuring the numerical model. Firstly, it is computationally expensive to simulate the full-sized 3-D wave flume. Therefore, the dimensions of the numerical wave flume are optimized in order to minimize computational costs while maintaining accuracy in the flow field (aiming for the same surface elevation and velocity). Secondly, with regard to the structural solver, although the cylinder exhibits minor deformations in the neutral posture during experiments, it is configured with a (straight upright) neutral vertical posture in the numerical model.

The following section proposes a framework for simulating the swaying of flexible elements under wave action, with a particular focus on the separate consideration of structural dynamics and hydrodynamics. Subsequently, the coupled interactions between these two phenomena will be investigated.

For the hydrodynamics, a numerical wave flume (excluding the flexible cylinder) is employed to evaluate the wave field, thereby ensuring the propagation of waves in accordance with the specified conditions in the experiments.

With regard to the structural solver, three standalone tests are proposed as a preliminary step before incorporating the flexible cylinder into the wave tank. The objectives of these tests are: firstly, to validate the structural solver against benchmark data (analytical solutions of a cantilever beam), and secondly, to ensure the stability of the coupling by simulating the flexible structure in a hydrostatic environment. After the completion of these tests, the numerical wave flume is configured with a flexible cylinder, and the results are compared to the experimental data. Figure 2 provides a graphical representation of the described framework.
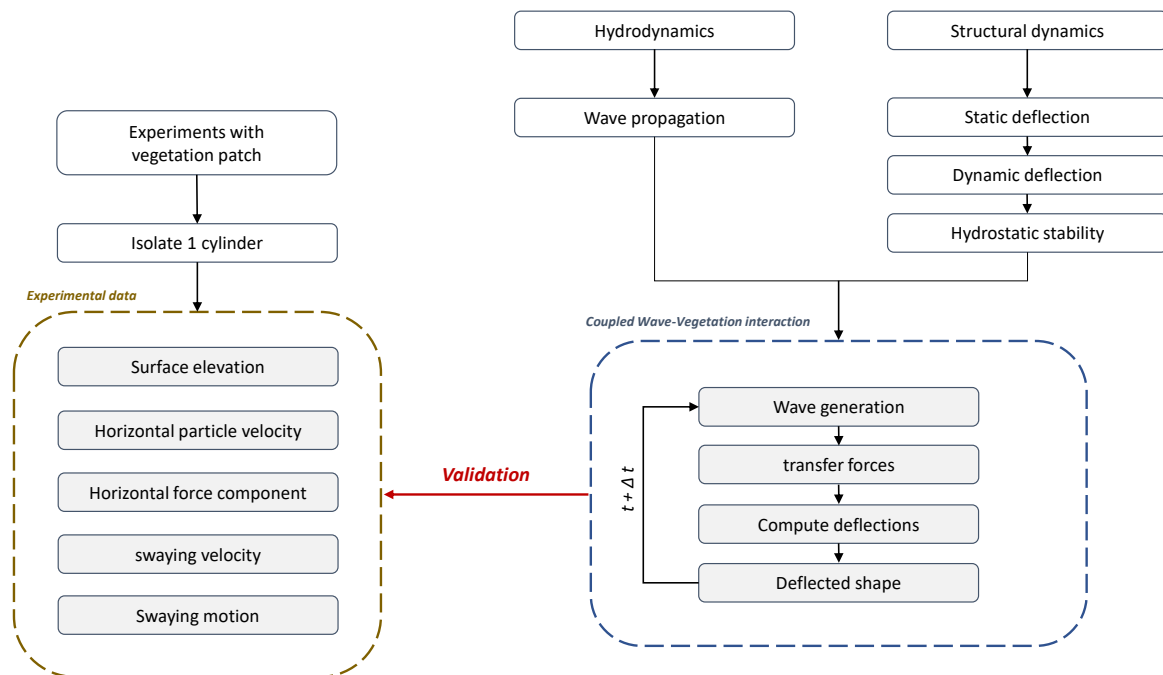

Figure 2. Schematic illustrating the proposed framework for numerically simulating the flexible cylinder deflecting under the action of waves. The right panel of the chart details the numerical approach. The numerical results are validated against experimental data.

The initial objective, as outlined in the proposed framework, is to confirm the stability and accuracy of the FEA solver (in this case the Euler beam element in Chrono) in solving the dynamics of the beam in a dry environment. The test configuration involves a typical setup of a cantilever beam, fixed at one end and free at the other (refer to Figure 3). This configuration follows established practices for validating structural models in studies involving fluid–structure interaction, as described in [42,54–56]. The geometric and mechanical properties of the flexible beam, as reported in the experiments (see Table 1), are used to configure the numerical model and test a static and a dynamic environment. Figure 3 presents both test cases. In the static environment (top panel), the beam is subjected to a dead load *q(x)*, and in the dynamic environment, an initial velocity function *v(x)* is imposed on the beam, which is free to oscillate over time (gravity is disabled in this scenario). The results of the numerical simulations can then be compared to the standard analytical solutions presented in what follows.
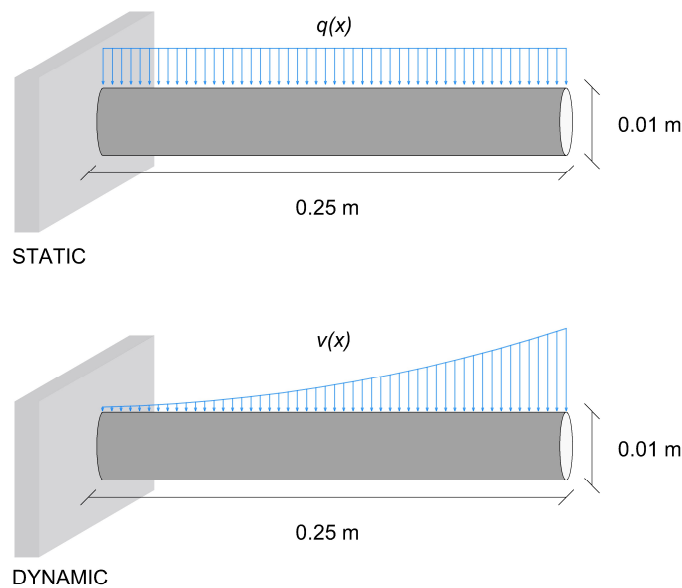

Figure 3. Setup for the static (**top**) and dynamic (**bottom**) tests performed on the cantilever cylinder clamped at one end and free at the other. The initial conditions are represented using blue arrows referring to a uniform load *q(x)* for the static test and an initial velocity distribution *v(x)* for the dynamic test.

For the static environment, the maximum deflection $\delta(x)$ can be calculated as:

$$\delta(x) = \frac{qL^2x^2}{4EI} - \frac{qLx^3}{6EI} + \frac{qx^4}{24EI} \tag{7}$$

with *q* being the dead load of the beam, *L* the length, and *EI* the flexural rigidity being the product of the Young's modulus (*E*) and moment of inertia (*I*).

For the dynamic environment, the beam is subjected to an initial velocity distribution, *v(z)*:

$$v(x) = \xi c_s \frac{f(x)}{f(L)} \tag{8}$$

where $\xi = 0.01$ and c_s is the speed of sound. The function *f(x)* is calculated according to:

$$f(x) = (cosk_wL + coshk_wL)(coshk_w - cosk_wx)$$
$$+ (sink_wL - sinhk_wL)(sinhk_wx - sink_wx) \tag{9}$$

with k_wL being equal to 1.875 (first mode of vibration). The frequency of the induced oscillations can be estimated according to:

$$w_1 = (k_w L)^2 \frac{1}{L^2} \sqrt{\frac{EI}{\rho A}} \tag{10}$$

Finally, the solution for free oscillations at the free end can be calculated using:

$$\delta_1(x, t) = \frac{\xi c}{w_1} sin(w_1 t) \tag{11}$$

The second step in testing the stability of the structural solver involves the use of the static water tank shown in Figure 4. This setup consists of a cubic water tank with a still water level and a flexible cylinder positioned at the center. The water depth and the properties of the cylinder are identical to what is reported in the experiments. Additionally, a sufficient distance is maintained between the cylinder and the walls of the tank to avoid any interference with the boundaries. This setup serves as a numerically efficient 3-D case that aims to ensure that the wave–vegetation coupling technique is stable, by assessing the accurate representation of the forces in hydrostatic conditions. The goal of running this case is to check the stability of the flexible element and posture under hydrostatic conditions. In comparing the output of the model to analytical solutions, the horizontal component of the transferred force is expected to be null, and the vertical force component should be equal to the net buoyancy force calculated as follows:

$$F_B = \rho^* g V \tag{12}$$

where ρ^* is the difference in density between the water and the cylinder, g is the gravitational acceleration, and V is the volume of the cylinder.
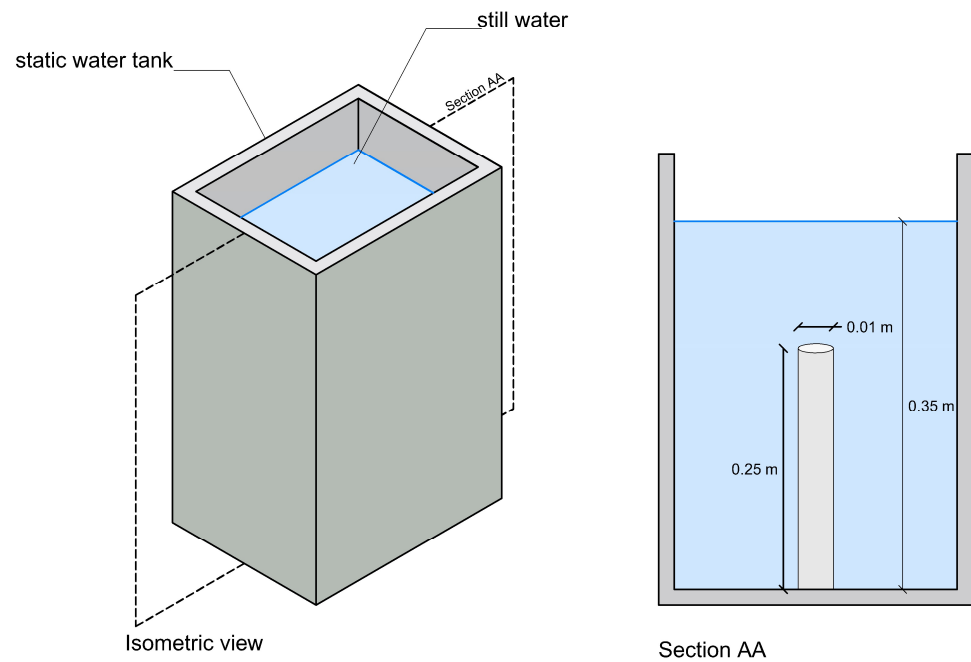

Figure 4. Isometric view of the static water tank used for hydrostatic testing, featuring a central flexible cylinder within boundary walls. *Section AA* provides a plan view for a clear depiction of cylinder dimensions and placement.

In the last step of the proposed framework (coupled wave–vegetation interaction), the objective is to replicate the experimental setup within a numerical wave flume. Figure 5 provides a sketch of the numerical wave flume employed in this study. This flume comprises a wave paddle for wave generation and a sloping beach (around 2-in-10 slope) for absorption. Furthermore, the absorption capacity is enhanced by the inclusion of a velocity damping layer, as indicated in the hatched partition of Figure 5.
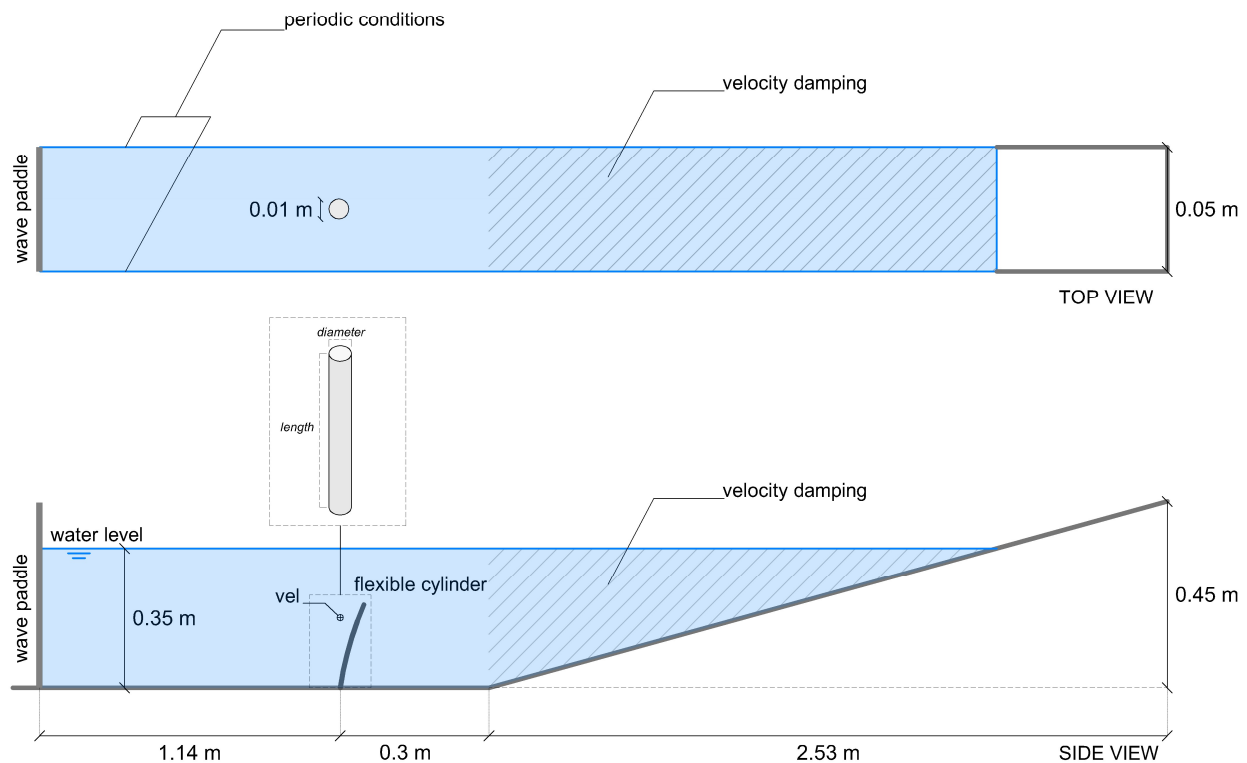
Figure 5. Configuration of the numerical wave flume employed in this study, featuring a piston-type paddle for wave generation, a beach with numerical damping (highlighted with diagonal hatching), and a central flexible cylinder. Periodic boundary conditions control the tank's lateral extents.

While a false bottom with a connecting concrete slope is a fundamental component of the experimental setup for instrument installation, these elements can be disregarded in the numerical model. Consequently, a straight bottom is maintained at both the wave generation and flexible cylinder locations.

Moreover, an additional 0.30 m is maintained downstream of the flexible cylinder as a buffer zone. The buffer zone serves to minimize interference from the wave absorption beach and velocity damping area. On both sides of the flume, a distance of 2 diameters (*D*) is maintained between the edge of the cylinder and the lateral periodic boundary conditions.

The numerical measurement setup is in accordance with the experimental description, featuring a wave gauge and a velocity meter positioned at the location of the flexible cylinder. The velocity meter is situated at a depth, *z*, of 0.175 m. The temporal dimension is also reduced: in the experiments, a generation time (T0) of 200 s is utilized, but this is subsequently reduced in the numerical model. The duration is selected to include a sufficient spin-up period and a fully developed wave field that exhibits a periodic cyclic motion.

It is important to emphasize that in the experiments, wave transformations cause deviations between the conditions generated at the paddle and those recorded at the location of the central cylinder. Wave transformations can be attributed to: (1) the false bottom with the concrete slope, and (2) the vegetation patch upstream of the central flexible cylinder. Thus, the measured water surface elevation at the central flexible cylinder location is used to establish the target wave conditions for the numerical model.

5. Results: Experiments and Numerical Simulations

The modeling framework previously outlined is applied in this section. Furthermore, the experimental results are presented. The numerical output is subsequently compared to the experimental data and conclusions are made. This section adheres to the framework's structure, starting with dry and wet testing for structural dynamics, followed by hydrody-

namics, and concluding with the coupled model. Throughout the stages of this procedure, various resolutions of the numerical model are considered to guarantee convergence.

5.1. Structural Dynamics

In the initial step, the static environment is considered. The deflection profile along the length of the beam is computed numerically and compared to the analytical solution as described in Section 4. In the numerical setup, two variables are considered. The first variable is the SPH resolution, which is calculated relative to the cylinder diameter D. The second is the discretization in the FEA module, which is represented by the number of beam segments. From the SPH standpoint, the objective is to demonstrate that the deflection profile is accurately captured across all three presented resolutions: (i) $dp = D/4$, (ii) $dp = D/5$, and (iii) $dp = D/6$. These resolutions represent the initial inter-particle distance (dp) that discretizes the cylinder with four, five, and six particles along the diameter (D) of the cylinder. From the FEA standpoint, the objective is to examine the accuracy across the three structural resolutions presented: (i) $N = 5$ segments, (ii) $N = 10$ segments, and (iii) $N = 20$ segments.

The results are presented in Figure 6, which depicts the normalized deflection along the length of the beam for various SPH and structural resolutions, plotted against the analytical solution. Remarkably, the results obtained across all combinations of three SPH resolutions and three FEA discretizations are in exact agreement with the analytical solution. This observation indicates that in a dry environment, the SPH resolution has no influence on the structural solver. Furthermore, the output of the FEA module converges from a low resolution.
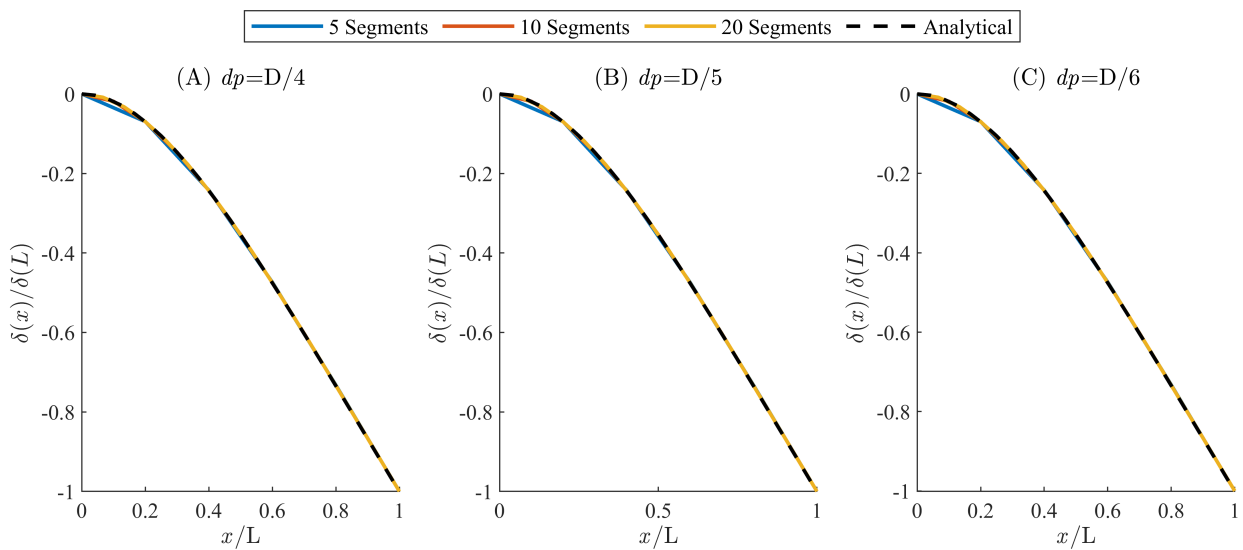

Figure 6. Comparing maximum deflection profiles along the cantilever beam for varying SPH resolutions and beam segment discretizations: plot (**A**) illustrates results from an SPH simulation with a resolution, *dp*, equivalent to diameter (*D*) divided by 4, while plot (**B**) represents the results for a resolution of diameter (*D*) divided by 5, and (**C**) represents the results for a resolution of diameter (*D*) divided by 6. The number of segments can be identified using the color palette. For comparison, the analytical solution is displayed using a dashed line.

In the dynamic environment, the cantilever beam is subjected to an initial velocity function that induces an oscillatory motion. This motion can be analytically resolved using the equations presented in Section 4. While the velocity function, *v(x)*, is continuous in space over the length of the beam, *L*, in the SPH domain, the initial velocity can be exclusively applied at the nodes connecting the segments. For a setup with *N* segments, the structural element includes *N* + 1 nodes. This implies that the numerically applied initial condition only converges to the function *v(x)* as *N* tends to infinity. However, in practical terms, configurations with *N* = 10 and *N* = 20 can sufficiently represent *v(x)*,

allowing for the recreation of the analytical oscillations [42,54]. The results for $N = 10$ and $N = 20$ are presented in Figure 7. The tip deflection, δ, at time instant, t, is normalized by the maximum tip deflection, $\delta(L)$, and plotted over a total duration of 5 s. The results show that the oscillations are accurately simulated with a 3% error in amplitude and a 1% error in period. The natural oscillating frequency of the beam is 0.90 s numerically and 0.91 s analytically.
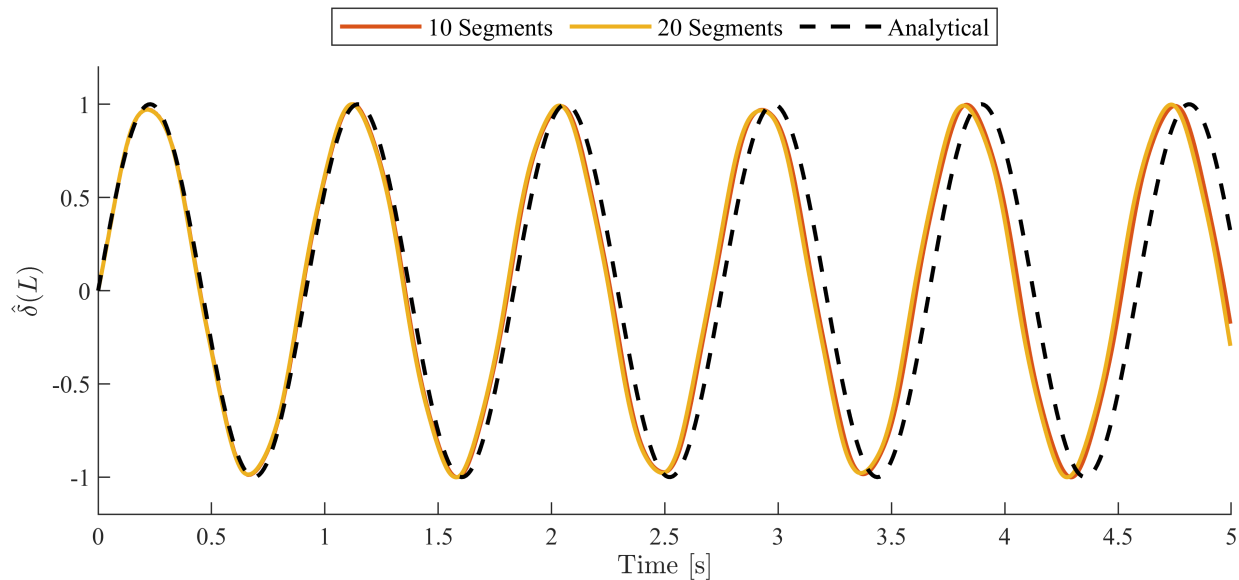

Figure 7. Normalized tip deflection, $\hat{\delta}(L)$, of the oscillating beam over time. The simulation spans 5 wave cycles, depicting the analytical solution with a black dashed line. A solid color legend is used to distinguish the number of segments used in the numerical simulations.

5.2. Hydrostatic Stability

The final check performed before transitioning to the numerical wave flume is ensuring the stability of the flexible cylinder in the static water tank. A simulation with a total duration of 2 s is performed using the setup shown in Figure 4. The results are presented across three SPH resolutions, $dp = D/4$, $dp = D/5$, and $dp = D/6$, as illustrated in Figure 8. In all three resolutions, the structural resolution, indicated by the number of segments N, is set to 10. The results of this simulation are interpreted through the transferred force, F_{trans}, visualized through a horizontal and vertical component, with the latter representing the net buoyancy force (analytically calculated using Equation (10)). This buoyancy force is depicted using a dashed black line in the left panel of Figure 8. The numerically calculated resultant buoyancy force across all three SPH resolutions is differentiated using the color palette. Consistently, the vertical component in the numerical model remains positive. This is significant as it verifies the inclusion of physics related to the density contrast between the cylinder and the surrounding fluid. The buoyancy force plays a crucial role; firstly, it enhances stability, and secondly, it potentially influences the cylinder's reconfiguration when swaying under wave flow. Concerning the magnitude, the buoyant force is initially overestimated by 0.02 N in the $D/4$ simulation, but the solution eventually converges to a value of 0.13 N with the higher $D/5$ and $D/6$ resolutions. Moreover, the initial high frequency noise present in the system fades out towards 1.5 s into the simulation. This provides an indication of the necessary spin-up duration for setting up simulations involving waves. Ideally, the initial interactions between the waves and the flexible cylinder should occur once the initial noise has dissipated. With regard to the horizontal component depicted in the right panel of Figure 8, a null vector indicates an equilibrium in the system, demonstrating that the flexible cylinder maintains a neutral posture. This serves as evidence that the force transfer along the fluid–structure interface is accurate and appropriately distributed.
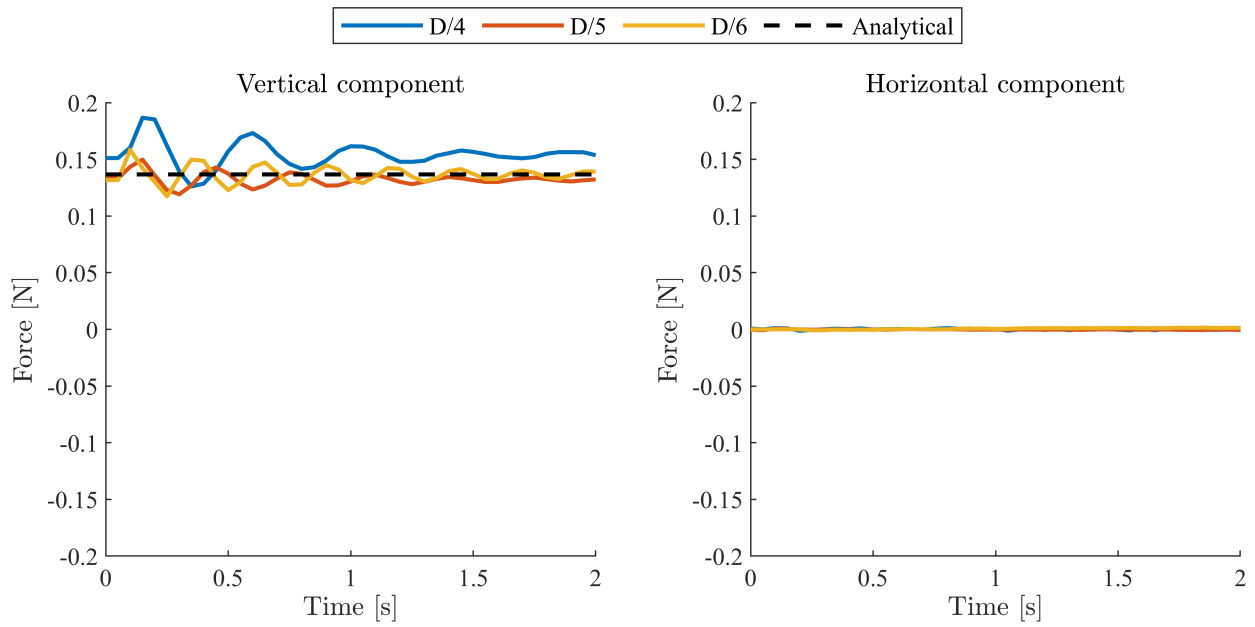
Figure 8. Vertical and horizontal components of the force transfer under hydrostatic conditions.

5.3. Wave Propagation

The experimental surface elevation at the location of the flexible cylinder being analyzed in this study is shown in Figure 9. The recorded surface elevation is represented by two shades of color: a light crimson shade for ramp up and ramp down, and a bold crimson color for the regular periodic state (comprising 55 waves analyzed in this study). Additionally, the velocities are recorded at the location of the flexible cylinder ($z = 0.175$ m) and shown in the bottom plot of Figure 9. Similarly, a bold shade is used for the regular periodic state.
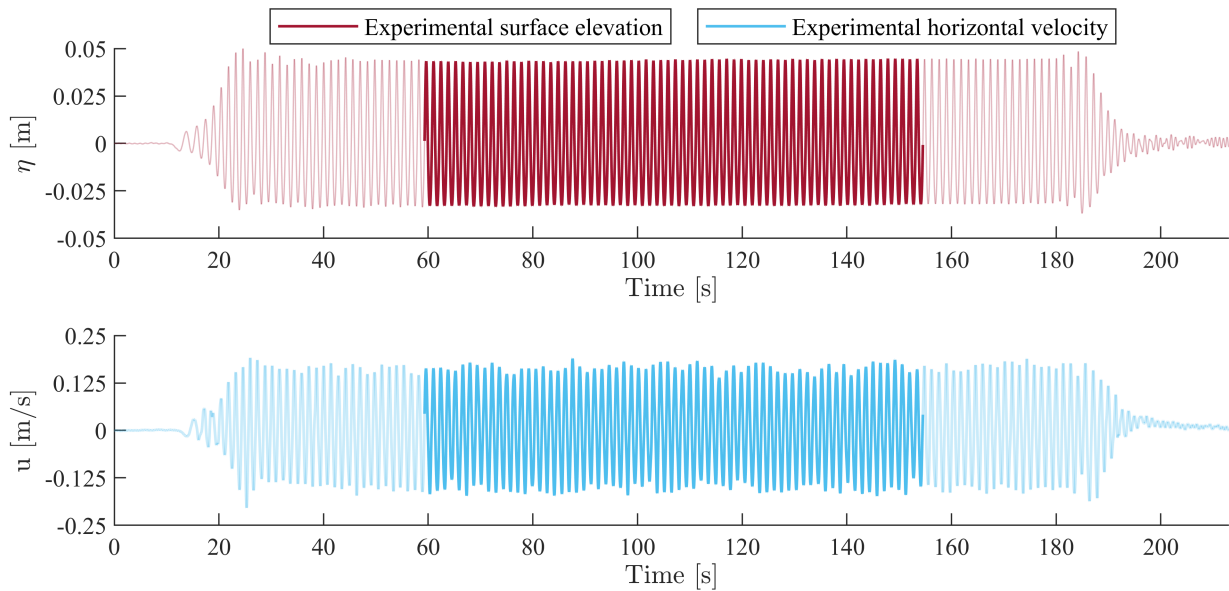

Figure 9. Experimental data for the surface elevation and the horizontal water velocity component. Acquired data during the experiment are plotted using a light shade, while a bold shade highlights the data segment used in this research.

The surface elevation data obtained from the experimental analysis (periodic state, bold crimson in Figure 9) are phase-averaged to generate the target wave conditions (wave conditions at the location of the flexible cylinder). In the experimental test, the generated waves transform due to the false bottom, connecting slope, and upstream array of cylinders, leading to target wave conditions with a wave height, H = 0.076 m, and wave period, T = 1.40 s. These target wave conditions are used to force the numerical wave paddle in order to achieve hydrodynamic conditions (surface elevation and velocity) identical to those observed in the experiments.

The wave propagation is calibrated using the wave tank shown in Figure 5 for three SPH resolutions: $D/4$, $D/5$, and $D/6$. The total duration of the simulation is set to 10 s, which is sufficient to include an initial spin-up period of 2 s and then deliver a fully developed state consisting of four wave cycles. The duration of the spin-up is selected based on the vertical and horizontal force transfer components examined in the hydrostatic tank (refer to Section 5.2). Additionally, a smoothing function is used to ramp up the wave paddle displacement. The described setup adds up to 4 million particles for the lowest resolution and 14 million particles for the highest resolution. The computational time spans from 20 h to 90 h on a GPU NVIDIA A100-SXM4 80 GB.

The results for the surface elevation, as calculated in the SPH simulations, are presented in Figure 10. A color legend is used to distinguish the SPH resolutions, and for comparison, an extract from the fully developed experimental data is added to the plot using the crimson color. In addition, the surface elevation for the target wave conditions is calculated using Stokes second order theory and added to the plot for reference. The agreement in amplitude and period between the three SPH simulations and the experimental data is evident from the overlapping plots depicted in Figure 10. The zoomed-in hatching displays the misalignment that is in the order of 10^{-3} m, or 0.25% error in amplitude.
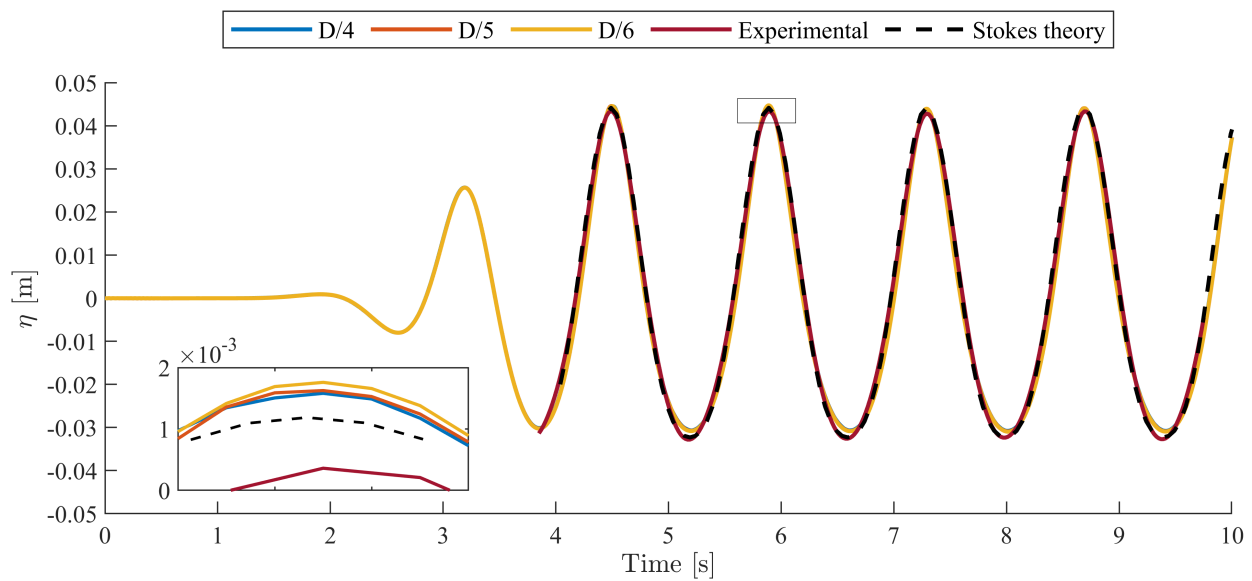

Figure 10. Comparing SPH results for surface elevation at the flexible cylinder location across three resolutions with experimental data and Stokes theory. A zoomed-in hatching is employed to illustrate the alignment at a scale of 10^{-3} m.

The phase-averaged results obtained from the fully developed fields in the SPH simulations are calculated and plotted against the phase-averaged experimental results in Figure 11. The results demonstrate that the numerical simulations converge across all three resolutions. It can be observed that the blue and orange colors, which represent the $D/4$ and $D/5$ simulations, respectively, are overlapped by the yellow plot corresponding to the $D/6$ simulation. A comparison of the numerical and experimental results reveals that both exhibit an identical period of 1.39 s. In terms of magnitude, the crest of the numerical waves

sits at 0.045 m, while the experimental waves are at 0.044 m. The misalignment increases along the trough, where the numerical surface elevation is −0.029 m and the experimental is −0.032 m.
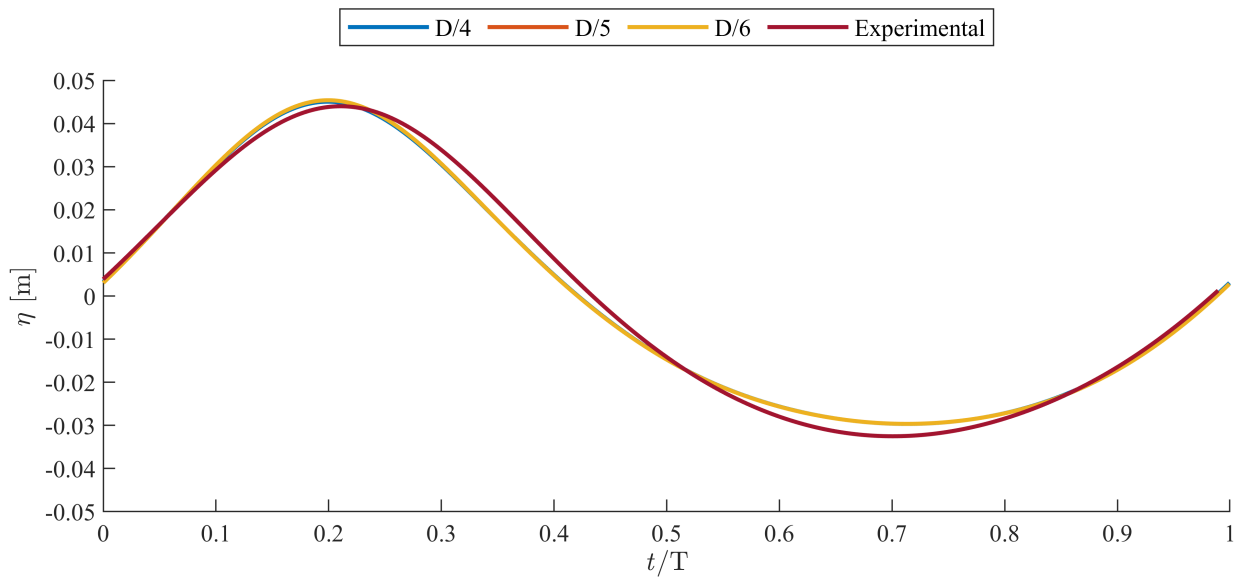
Figure 11. Phase-averaged SPH results for surface elevation plotted over a single cycle and compared to experimental data. SPH resolutions are represented using a color palette.

Furthermore, a comparison is conducted for the horizontal water velocity at the point equivalent to $z = 0.175$ m along the water column, as illustrated in Figure 12. The horizontal velocity across all SPH resolutions is perfectly convergent and aligns in terms of period. The amplitude of the numerical data remains consistent across all waves, whereas the experimental data appear to fluctuate more from one cycle to another. Finally, a comparison of the numerical and experimental results with Stokes second order theory, plotted using the black dashed line, reveals a misalignment of approximately 10^{-2} ms^{-1}, or 5% in amplitude.
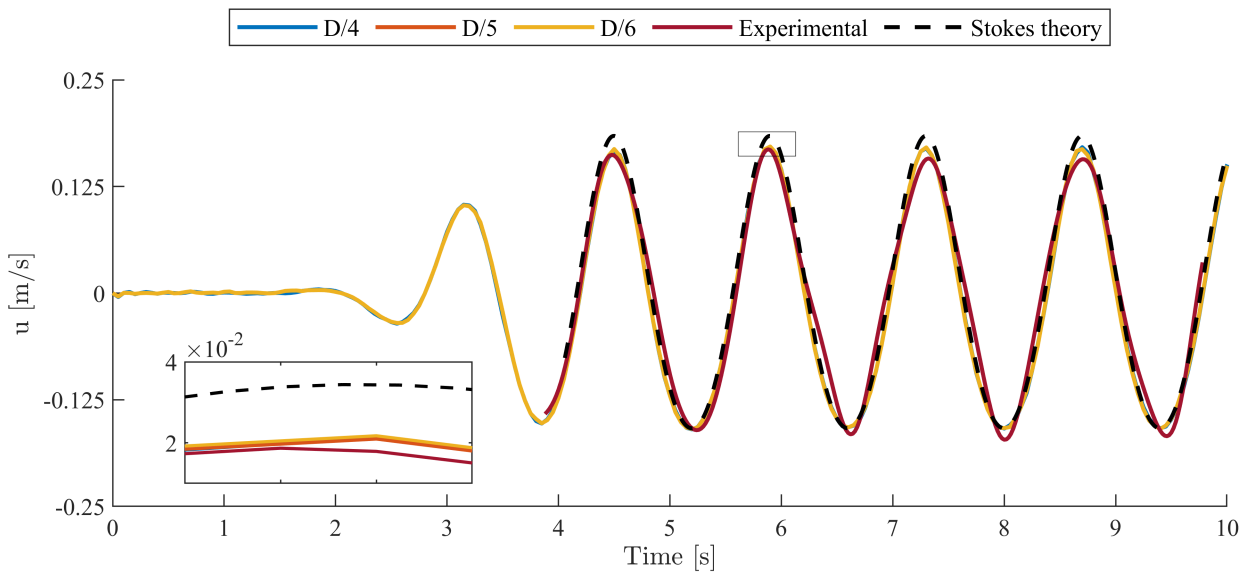
Figure 12. Comparing SPH results for horizontal water velocity at the flexible cylinder location across three resolutions with experimental data and Stokes theory. A zoomed-in hatching is employed to illustrate the alignment at a scale of 10^{-2} m. The data are acquired at $z = 0.175$ m equivalent to the center point along the water column.

The numerical model successfully replicates the experimental hydrodynamic forcing, including surface elevation and the horizontal velocity component, across all resolutions analyzed in the SPH output. The misalignment between the results and the experimental data is within tolerable margins in terms of both amplitude and period. These hydrodynamic results validate the applicability of the proposed method used in this study, where the conditions at the center of a vegetation patch are recorded and replicated numerically. With the hydrodynamic forcing validated, the subsequent sections explore the dynamics of the flexible cylinder. A snapshot of the numerical output is shown in Figure 13.
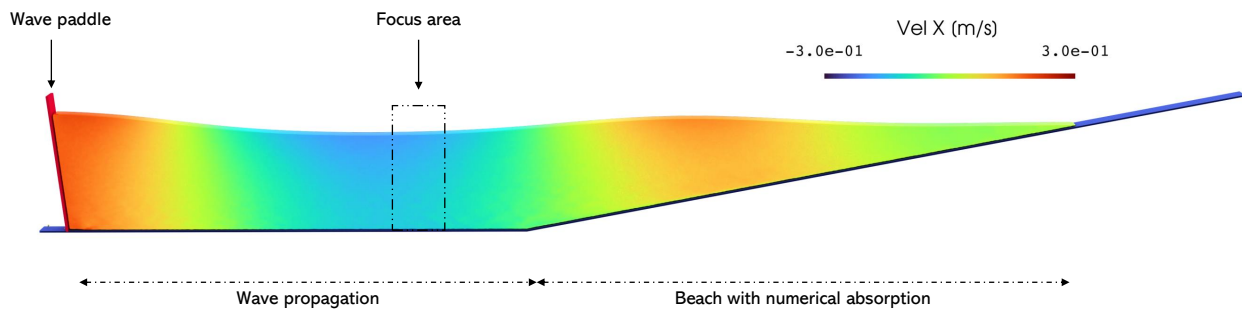

Figure 13. Snapshot of the numerical simulation: visualizing the horizontal water velocity with a color jet map.

5.4. Wave–Vegetation Interaction

The wave–vegetation interaction is experimentally studied using the setup consisting of a wave flume and a flexible cylinder. Numerically, after validating both the structural dynamics and the hydrodynamics in Sections 5.1–5.3, the next step uses the identical wave tank used for the hydrodynamic validation, presented in Figure 5, with a flexible cylinder situated at half a wavelength away from the wave paddle. The cylinder characteristics as reported in the experiments (see Table 1) are again used. To confirm the convergence of the solution, three SPH resolutions are used to run the simulations for a total duration of 10 s. The cylinder discretization in the structural solver remains constant at $N = 10$ segments throughout.

The following section presents a detailed analysis of the transfer of forces and the swaying motion of the flexible cylinder, as reported in the experiments and as simulated in the numerical model.

Force

The interactions between the waves and the flexible cylinder can be evaluated through the horizontal force component, F_x, that is, in turn, an indicator of the interactions between the waves and the cylinder. The force signal was recorded throughout the whole duration of the experiment as presented in Figure 14. In the top panel, the light shade of crimson represents the ramp-up and ramp-down periods, while a bold shade is used to highlight the dataset used for comparison with the numerical model (corresponding in time to same bold shade presented for surface elevation and velocity in Section 5.3). As anticipated, the recorded force, F_x, exhibits an oscillatory nature with maximum and minimum values $F_{xmax} = 0.034$ N and $F_{xmin} = -0.027$ N (calculated as the average maxima (F_{xmax}) and minima (F_{xmin}) of the 55 cycles highlighted using the bold color). Theoretically, force is linked to the horizontal flow velocity (Morison equation, [35]), and given that the cylinder is forced by oscillatory waves of second order, where the velocity is positively dominant (maximum positive value is larger than negative value), it is expected to obtain larger positive forces.

The spectral analysis of the signal, obtained through a Fast Fourier Transformation (FFT), is illustrated in the lower panel of Figure 14. The signal shows the dominant component with the largest amplitude and frequency of 0.71 Hz, exactly coinciding with the wave frequency of 0.71 Hz (wave period is 1.40 s). Thus, it could be concluded that

the oscillatory flow is the only force present in the system, with no evidence of vibrational forces resulting from the dynamic effects observed.
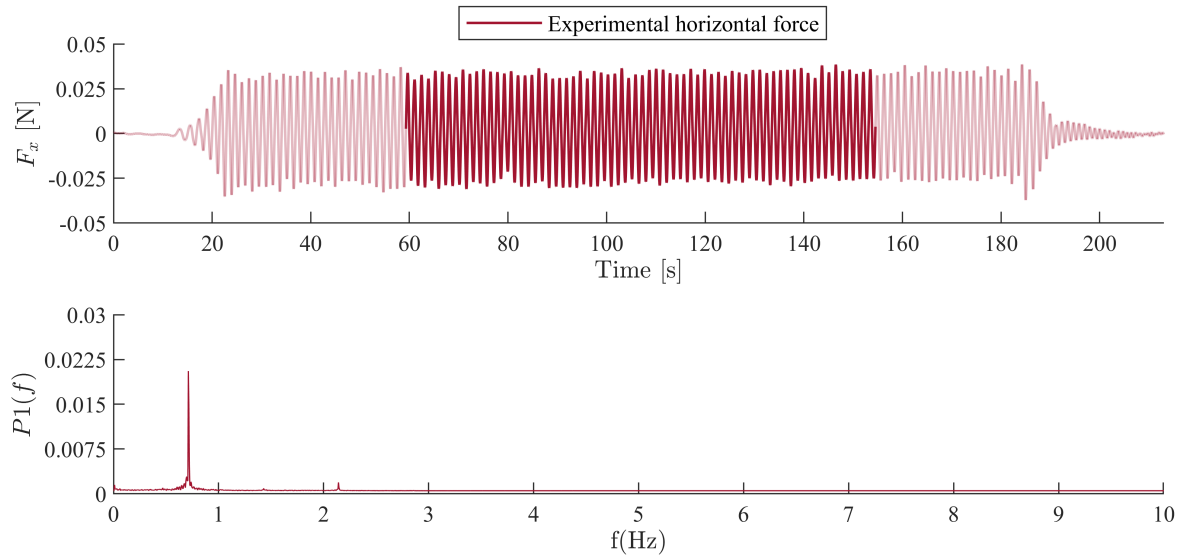

Figure 14. Experimental data for the horizontal force component: the top panel displays the experimental data for the total length of the experimental test, plotted using a light shade, while highlighted in bold shade is the data segment used in this study. The bottom panel showcases the spectral analysis of the signal.

The simulations are performed using a numerical wave flume that is identical to the setup used for validating the hydrodynamics (Section 5.3). The flexible cylinder is configured according to the reported characteristics in Table 1, exactly resembling the setup detailed in the structural validation (Section 5.1). The simulation is executed for a total duration of 10 s, to accommodate an initial spin-up period of 2 s followed by a wave generation smoothing function and four full wave cycles. The results of the simulations referring to the three SPH resolutions tested, $D/4$, $D/5$, and $D/6$, are shown in Figure 15. In the top panel of Figure 15, the horizontal force component F_x, calculated as the sum of individual forces acting on each of the 10 segments, is plotted against time.
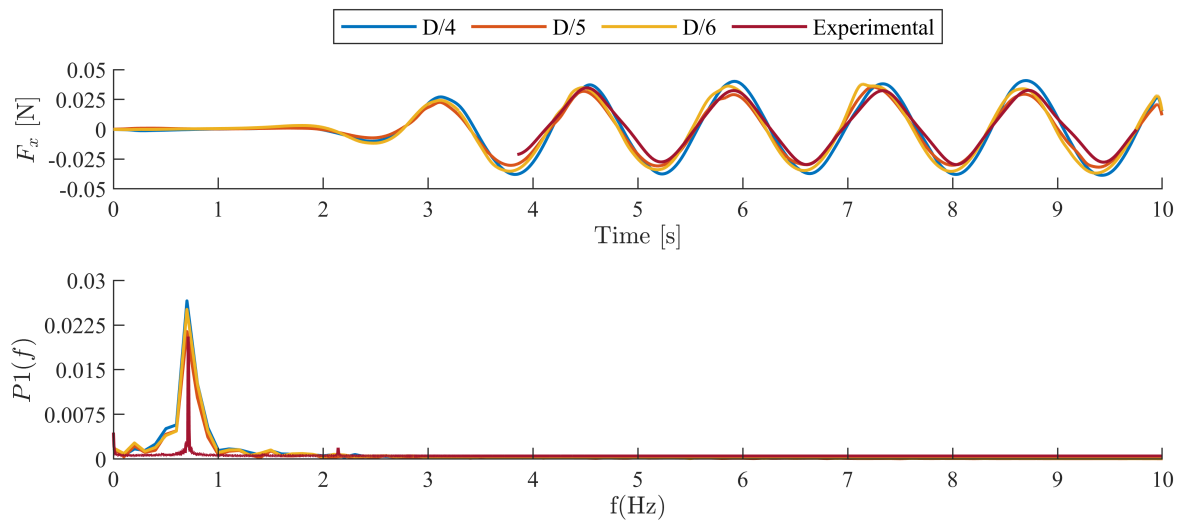

Figure 15. Comparing the SPH results to experimental data: the **top** panel illustrates the horizontal force component across three resolutions, alongside the experimental data. The **bottom** panel presents the spectral analysis of the signals.

As the waves interact with the flexible cylinder, the signal begins to increase in amplitude at approximately t = 2.5 s. This continues until the signal reaches a point of oscillatory nature, which persists for the remainder of the simulation. The numerical force, consistent across all three resolutions, closely mirrors the trend of the experimentally recorded force (shown in crimson in Figure 15). The peaks, troughs, and periods of the experimental force are captured with good accuracy for the four wave cycles analyzed. The maximum forces range from F_{xmax} = 0.031 N to 0.039 N, while the minimum forces range from F_{xmin} = −0.030 N to −0.037 N. Notably, the $D/4$ simulation exhibits the largest overestimation of both peaks and troughs. However, as the resolution increases to $D/5$ and $D/6$, the agreement between experimental and numerical data improves. These data are summarized in Table 2. The lowest discrepancy occurs at the highest resolution, with a peak overestimation of 0.001 N and a trough overestimation of 0.004 N, equivalent to errors of 3% and 1%, respectively. The quantitative error analysis is detailed through the root mean square error (RMSE) and mean average error (MAE) provided in Table 3. The numerical model consistently predicts the measured forces with mean errors ranging from 0.005 N to 0.007 N, which aligns with the discrepancies observed in capturing the maximum and minimum horizontal forces F_{xmin} and F_{xmax}. Additionally, RMSE, which is more sensitive to outliers, consistently exceeds MAE. This is likely due to the presence of outliers in the numerical force signal due to numerical noise amplified by the flow-induced vibrations in the structure.

Table 2. The maximum and minimum horizontal force on the flexible cylinder as recorded in the experiments and simulated in the simulations with resolutions D/4, D/5, and D/6.

	F_{xmax} [N]	F_{xmin} [N]
Experimental	0.034	−0.027
$D/4$	0.039	−0.037
$D/5$	0.031	−0.030
$D/6$	0.035	−0.031

Table 3. Numerical model performance for the horizontal force on the flexible cylinder is presented through: (1) RMSE, root mean square error, and (2) MAE, mean absolute error.

F_x	RMSE	MAE
$D/4$	0.007	0.006
$D/5$	0.006	0.005
$D/6$	0.008	0.007

The components of the numerical force are presented through the spectral analysis, as illustrated in the lower plot of Figure 15. The frequency of the dominant component is accurately captured in the numerical simulations and is in agreement with the experimental data. At a frequency of 0.71 Hz, the dominant force is confirmed to be applied by the waves. The amplitude of the $D/4$ simulation overshoots the experimental, $D/5$, and $D/6$ simulations. This is also reflected in the analysis of the maxima and minima.

In the literature, the FSI validation case presented in Turek and Hron [57] and simulated in O'Connor and Rogers [58] reinforces the trend of more accurately capturing forces with higher SPH resolutions. The proposed framework is of particular importance in this context, as the hydrodynamics have previously been validated and demonstrated convergence across all resolutions. Consequently, they can be excluded as a potential cause of discrepancy in the forces across resolutions. This enables a more focused investigation into other factors impacting the simulation results. Primarily, the boundary interface is better defined and resolved at higher resolutions.

5.5. Swaying Motion

In the context of wave–vegetation interaction, the swaying motion under the action of the oscillatory flow is of interest given the implications it has on the wave-attenuation potential and on the stem and meadow scale flow characteristics. The swaying motion is strongly coupled to two elements: one is the structural characteristics, which is the flexible cylinder in this case, and two is the forcing field, which is the hydrodynamic conditions and resulting force transfer. Given that both these elements have been accurately reproduced in the numerical simulation, the swaying motion of the flexible cylinder is expected to follow the experimental pattern. This section presents the experimental and numerical swaying motion, defined as the displacement of the tip along the horizontal *x*-plane and vertical *z*-plane.

A fixed camera feeding a post-processing video analysis script was used in the experimental setup to capture the displacements of the flexible cylinder at a rate of 50 Hz [45]. The results for the tip displacement are presented in Figure 16, where the horizontal (*X*) and vertical (*Z*) displacements are shown in the top and bottom panels, respectively. Across both displacement plots, the light shade represents the ramp-up and ramp-down, while the bold shade shows the data used for comparison. The horizontal (*X*) displacement reveals an oscillatory pattern with cycles ranging from maximum and minimum displacements of 0.053 m and −0.045 m (calculated as the average values across all 55 cycles). The resulting range of swaying, defined as the total distance covered by the tip during a wave cycle, is 0.098 m.
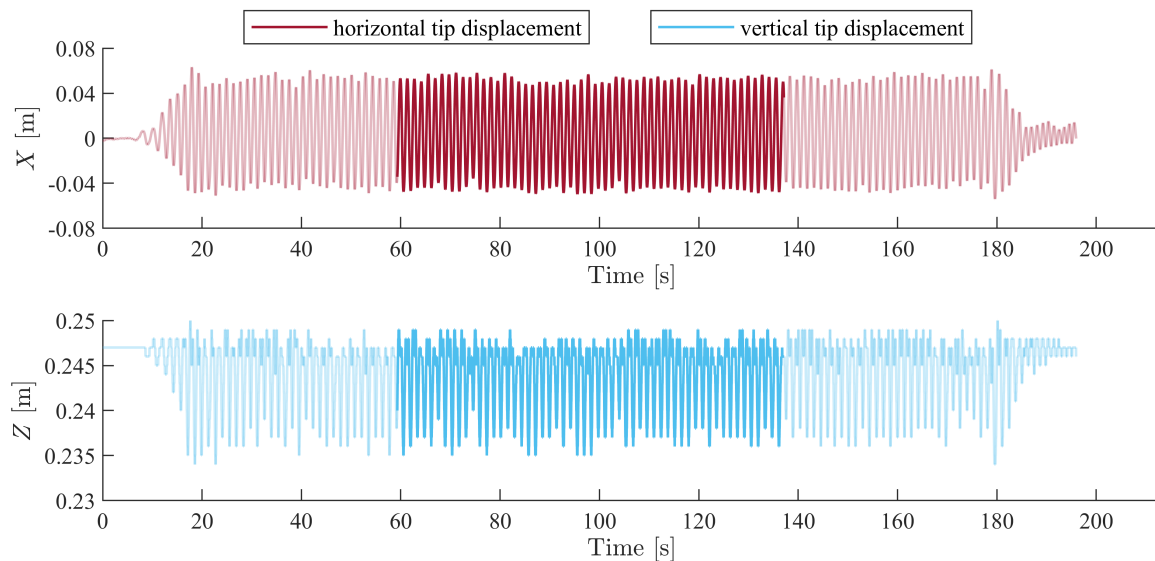

Figure 16. Experimental data for the horizontal and vertical tip displacements. The experimental data for the total duration of the experimental test are plotted using a light shade, while highlighted in bold shade is the data segment used in this study.

The numerical results obtained throughout the 10 s simulations for the three SPH resolutions, $D/4$, $D/5$, and $D/6$, are presented in Figure 17. The horizontal (*X*) displacement is plotted using three distinct color legends, and an extract of the experimental data is added for comparison. The visual agreement in period is evident with all three plots coinciding during the zero-crossing phase. In terms of amplitude, the maximum displacements are 0.058 m, 0.052 m, and 0.054 m, while the minimum displacements are −0.050 m, −0.048 m, and −0.049 m for the resolutions $D/4$, $D/5$, and $D/6$, respectively. These values lead to a range of swaying equivalent to 0.108 m for $D/4$, 0.100 m for $D/5$, and 0.103 m for $D/6$. These data are presented in Table 4.

While maximum displacements provide a descriptive measure of swaying motion, the overall model performance for all swaying cycles is evaluated quantitatively through error analysis, as presented in Table 5. The RMSE and MAE indicate that the numerical solution at all three resolutions accurately captures the swaying of the flexible cylinder, typically within a range of approximately 5 mm. Furthermore, the results demonstrate convergence of the numerical model across all resolutions, typically with discrepancies around 3 mm.

Table 4. The swaying characteristics of the flexible cylinder as recorded in the experiments and simulated in the $D/4$, $D/5$, and $D/6$ simulations.

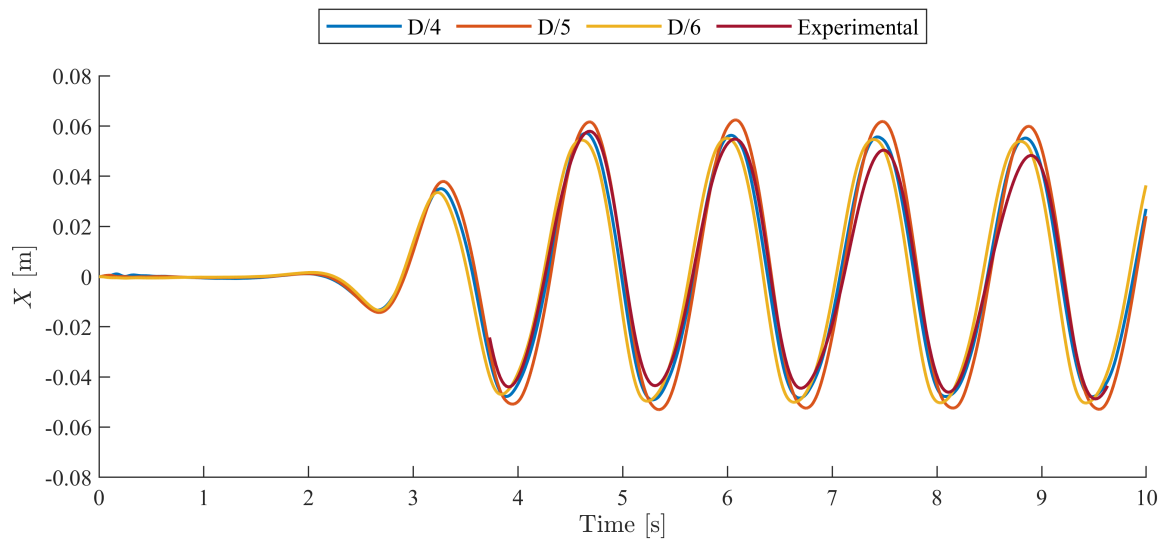|	X_{max} [m]	X_{min} [m]	$\overline{X}$ [m]
Experimental	0.053	−0.045	0.098
$D/4$	0.058	−0.050	0.108
$D/5$	0.052	−0.048	0.100
$D/6$	0.054	−0.049	0.103

Figure 17. Comparing SPH results, across three resolutions, for the horizontal (along the x-plane) swaying displacement of the flexible cylinder's tip to the experimental data.

Table 5. Numerical model performance for the horizontal swaying of the flexible cylinder is presented through: (1) RMSE, root mean square error, and (2) MAE, mean absolute error.

X	RMSE	MAE
$D/4$	0.006	0.005
$D/5$	0.004	0.003
$D/6$	0.003	0.002

The results indicate a discrepancy between the experimental data and the numerical models in the order of 10^{-4} m for the maximum and minimum swaying distances. This confirms the ability of the numerical model to properly capture the swaying behavior of the flexible cylinder. A notable aspect in the data is the larger swaying distance of the flexible cylinder with a resolution of $D/4$. This finding is consistent with the forcing data shown in Section 5.4 (refer to Figure 15), which shows larger local peaks for the $D/4$ resolution, that are in turn translated into larger swaying distances.

Recall how the forces presented in Section 5.4 demonstrated a dominant force component, which was positively oriented, as a consequence of the nature of the second order Stokes waves. This is also reflected in the swaying cycle of the flexible cylinder.

The maximum displacement is consistently larger in the forward (positive) direction in the numerical simulations, in line with the experimental data. Recall also how the spectral analysis showed a single major component with a frequency equal to the wave period, which is reflected into the swaying motion; the duration of the swaying cycle is equal to the wave period. In fact, the flexible cylinder sways at a frequency of 0.71 Hz in the experiments and 0.70 Hz in the numerical model. A discrepancy equivalent to 0.01 Hz equates to approximately a 1% error in cycle duration. This small misalignment is expected in the coupled system (fluid and structure) where the forcing term has a different frequency from the system response (natural frequency). This could be also exacerbated by the imposed numerical damping present in the Euler–Bernoulli beam configuration.

The swaying of the flexible cylinder can be converted into a posture plot, as shown in Figure 18. The numerical posture is compared to the phase-averaged experimental tip location, which is represented by the hollow crimson rings. For the numerical data, the posture is traced using lightly colored lines, and the location of the tip is indicated using scattered solid circles. The top left and top right panels, respectively, depict the results of the $D/4$ and $D/5$ resolutions, while the central bottom panel illustrates the results of the $D/6$ resolution. In accordance with the swaying distances detailed above (see Figure 17 and Table 4), the gap between the experimental and numerical swaying distances is noticeably narrower for the $D/5$ and $D/6$ simulations. Concerning the swaying characteristics within the numerical model, the pattern seems symmetrically shaped around the neutral (zero) posture but exhibits a greater magnitude towards the positive direction. On the other hand, the experimental data are also positively dominant, but they reveal a backward leaning swaying cycle that appears to plunge downwards ($-z$ direction) during the recoil swing and recovers upwards ($+z$ direction) during the forward swing. This is an expected outcome given the naturally deformed shape of the flexible rubber cylinder observed in the experiments. In contrast, this shape is assumed to be neutral when initializing the structural solver in the numerical model. The results also reveal that the cylinder sways under a single mode of deflection.
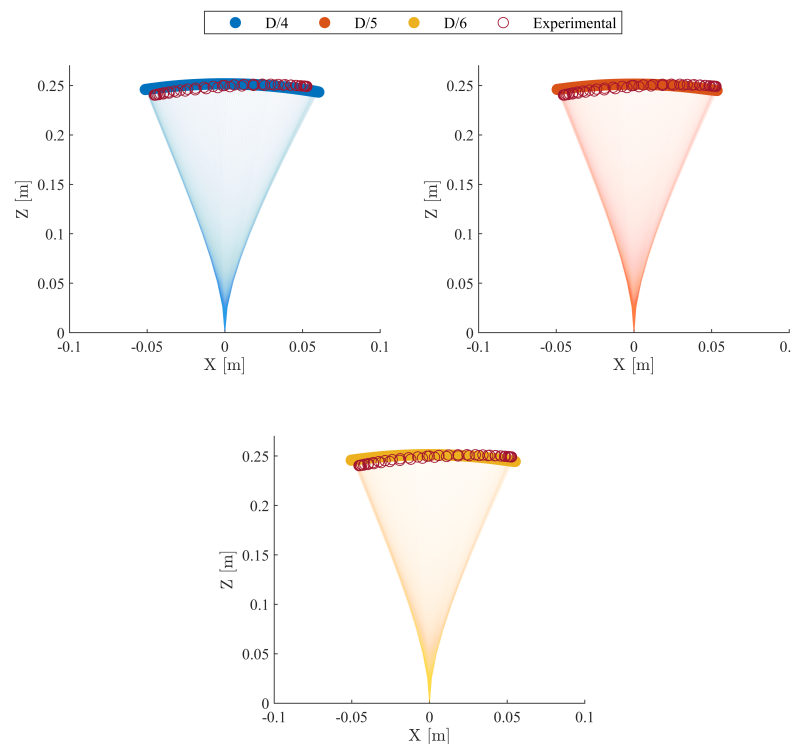

Figure 18. Posture plots for the flexible cylinder in the *XZ* plane. In the numerical data, a solid circle indicates the tip of the cylinder, while a light shade traces its length. Experimental tip locations are denoted by hollow rings for comparison.

Figure 19 illustrates the model output for the water surface and cylinder posture at five distinct timestamps. Beginning at timestamp $t/T = 0$, the cylinder is at its minimum deflection point and subsequently experiences an acceleration, changing direction under the wave crest at $t/T = 0.25$. Subsequently, the negative fluid velocity initiates the recoil spring to reach maximum negative deflection at $t/T = 0.75$. The cycle concludes as the cylinder returns to its starting position, marked by $t/T = 1$.
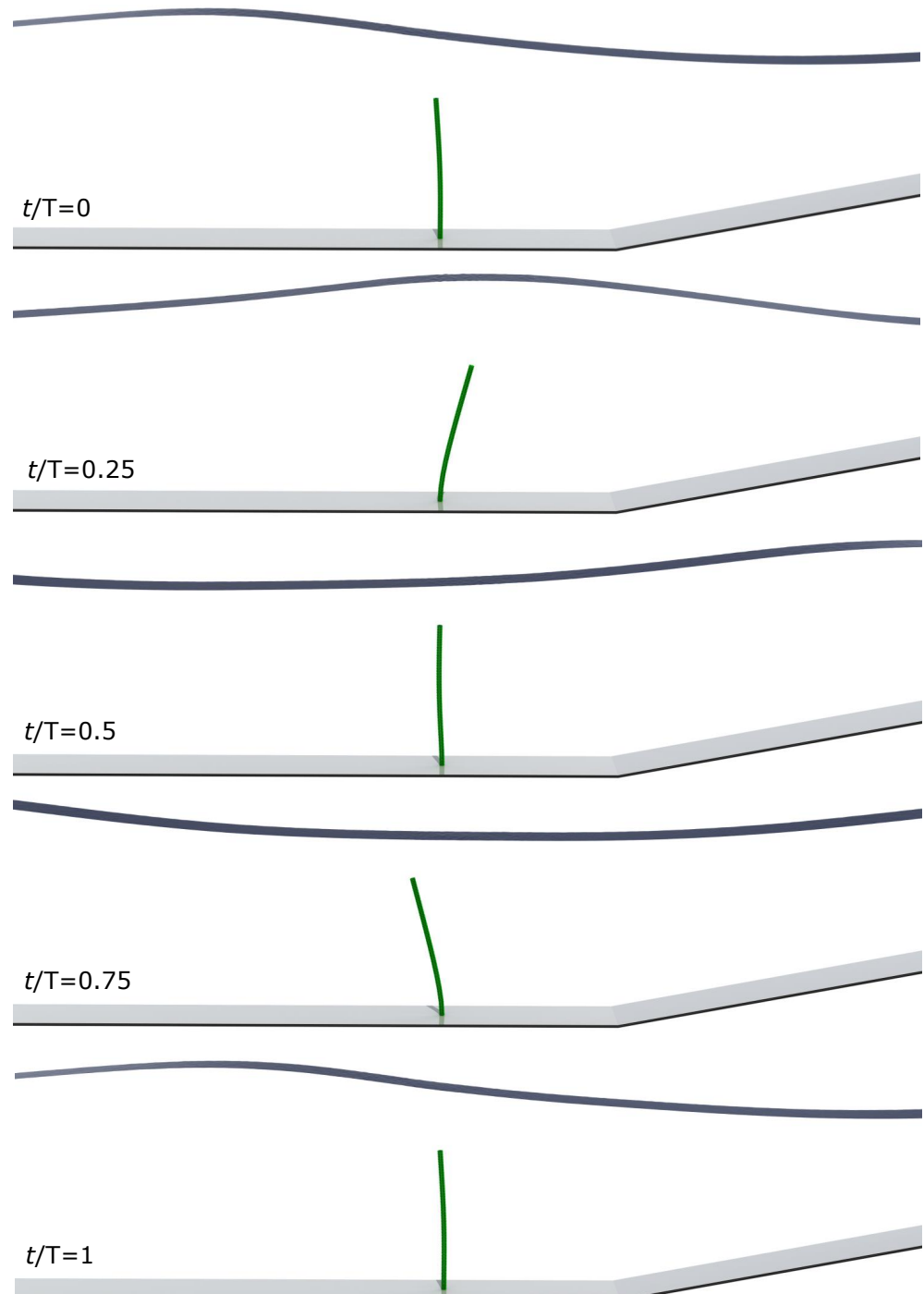

Figure 19. Visual rendering of the numerical simulations showcasing both the surface elevation (dark blue line) and the cylinder's posture at five distinct timestamps throughout a single wave cycle.

6. Discussion

While the establishment of a validated case and a functional numerical model is of paramount importance, the primary objective is to gain further insights and acquire data that may not be possible to obtain through laboratory experimentation alone. This section therefore sets out to revisit the previously presented framework and results in greater detail, with a particular focus on the swaying motion of the flexible cylinder and the uncovering of additional information concerning energy dissipation and vorticity generation.

6.1. Wave-Driven Swaying Characteristics

The swaying of the flexible cylinder results from hydrodynamic forcing, which surpasses the bending stiffness in magnitude and dominates over the buoyancy restoring force. This balance in the system can be characterized using a set of dimensionless parameters established in the study of Luhar and Nepf [34]. These parameters include the (i) Cauchy number (Ca), representing the ratio of hydrodynamic forcing to vegetation stiffness; (ii) the Buoyancy parameter, B, representing the ratio of buoyancy force to the vegetation stiffness; and (iii) the ratio of vegetation length to wave excursion, L_e. The corresponding values of these parameters are presented in Table 6. A value of L_e exceeding the established threshold of 1 (one) indicates that the vegetation sways within the range of the horizontal wave excursion. Recall from Section 5.5, the flexible cylinder's swaying distance is approximately 0.10 m, slightly larger than the calculated wave excursion of 0.08 m.

Table 6. Dimensionless parameters describing the swaying of the flexible cylinder. Calculation of these parameters follows the well-established equations presented in [34].

Cauchy number, Ca	11
Buoyancy parameter, B	21
Length to excursion, L_e	6
Keulegan–Carpenter number, KC	22
Reynold's number, Re	1536

Regarding force balance, the Cauchy number, Ca, is determined to be 11, which indicates that the hydrodynamic forcing is of a magnitude that is multiple orders of magnitude greater than that of the restoring force due to structural rigidity. It is noteworthy that the buoyancy parameter, B, is approximately twice the value of the Ca number. This might suggest that buoyancy is a dominant restoring force; however, further analysis reveals otherwise. Given the magnitude of buoyancy, approximately 0.13 N, compared to the recorded F_{xmax} of 0.034 N, it seems that the assumption of buoyancy dominance in the swaying and reconfiguration of the cylinder could be valid. However, since the deflection angle remains relatively small within the horizontal excursion limits, buoyancy plays no significant role under these conditions. Nevertheless, the importance of buoyancy in the system, particularly in numerical models with two-way coupling, should not be underestimated. The neutral posture of the cylinder in the experiments and the stability of the structural solver is enhanced by the upward-direction stabilizing buoyancy force.

Furthermore, the Reynolds number Re is presented to give an indication of the flow structure around the cylinder. With Re = 1536, the flow is in the subcritical regime and a vortex street is generated [59]. This is backed up by the Keulegan–Carpenter number KC, which is the ratio between the amplitude of the oscillatory flow and the diameter of the structure. A large KC = 22 indicates that inertia forces dominate over the viscous forces and the flow tends to separate in the form of vortex shedding [60].

The relative velocity between the flexible element and the surrounding water flow stands out as one of the most crucial links connecting stem-scale, meadow-scale, and ecosystem-scale models. Larger scale models rely on this velocity difference as a factor in drag dissipation (as seen in implementations such as those described in [23,61,62] on a larger scale). Stem-scale studies focus on this aspect, the relative velocity, and the swaying of vegetation throughout the cycle. Luhar and Nepf [34] proposed the use of an effective length approach, where flexibility

is overlooked entirely, and a stiff cylinder is used to generate forces equivalent to those of a flexible one. El Rahi et al. [39] also explored this topic, presenting the swaying velocities of the flexible element in a wave cycle. In their research, they suggest that the upper section of the flexible element sways passively at a speed relative to the wave's orbital velocity.

In order to gain insight into the swaying velocities and the relative speed between the structural element and the surrounding flow, the relative velocity between these two components throughout a single swaying cycle is presented in Figure 20. The swaying cycle is divided into two phases termed the forward swing and the recoil swing. The first phase represents the swaying from the minimum horizontal swaying distance and progresses in a clockwise direction (positive along the *x*-axis) towards the maximum, while the second phase represents the backward (negative along the *x*-axis) movement from the maximum swaying distance towards the minimum.
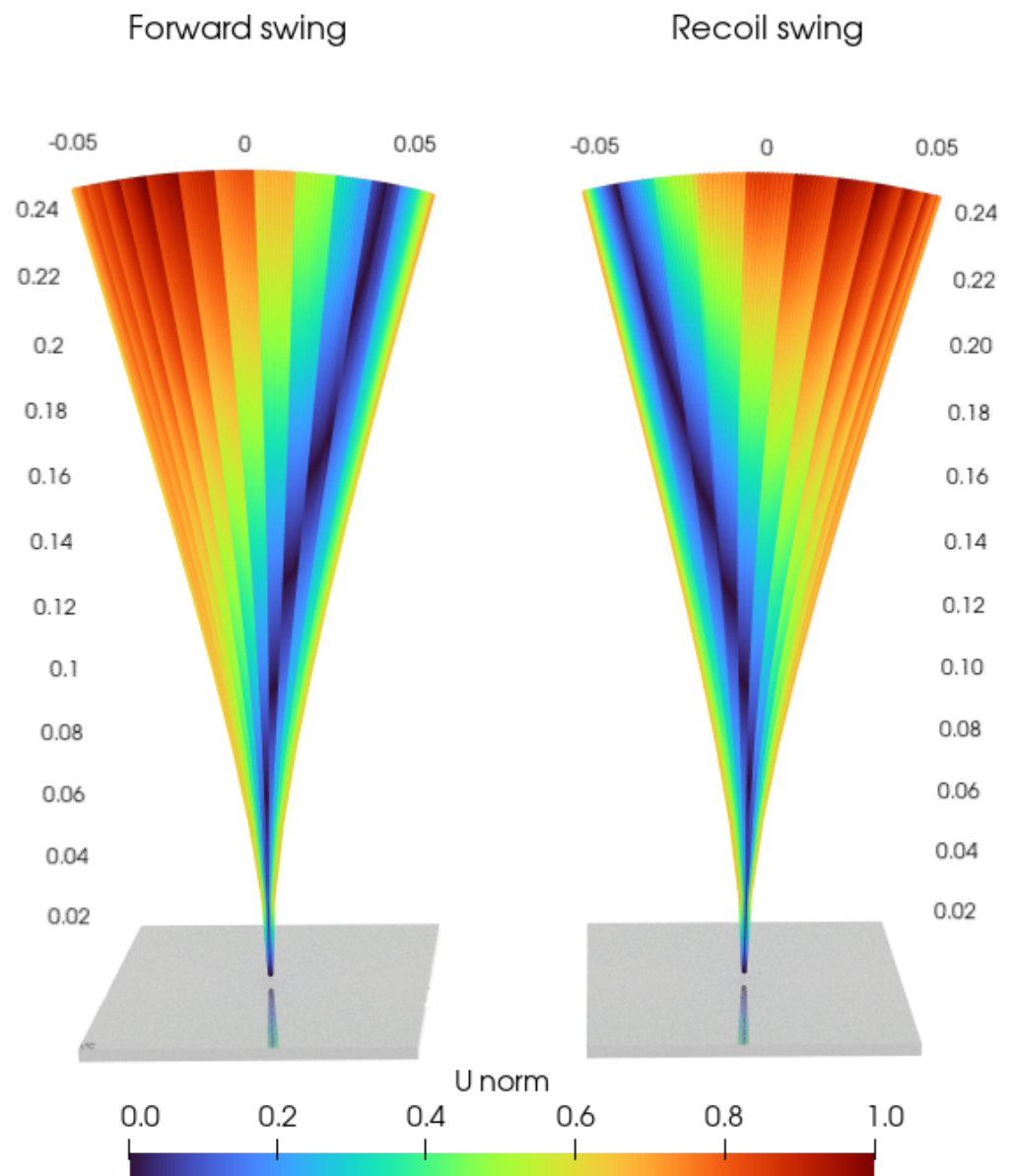

Figure 20. Sensu plot depicting the dynamics of a flexible cylinder during both the forward and recoil swings. The plot illustrates the relative velocity between the fluid and the cylinder. Spatially, the values are limited to locations where the cylinder is present during the simulation, resulting in the observed Sensu-like shape.

The Sensu plot displayed, which is named for its resemblance to the famous Japanese folding hand fan, illustrates the normalized horizontal velocity, denoted as U_{norm}. This velocity represents the normalized difference in horizontal velocity between the flexible cylinder and the surrounding flow. The colorbar ranges from 0 to 1, with 0 (dark blue) indicating an identical velocity and 1 (dark red) representing the maximum velocity difference.

Two conclusions can be drawn from this Sensu plot. Firstly, for the majority of the wave cycle, there is a variation in velocity between the cylinder and the flow. Secondly, the flexible cylinder only sways passively for a limited period of time (dark blue), twice during a single wave cycle. These instances occur briefly before the cylinder attains its maximum positive and maximum negative (Figure 19) deflected postures, at around $t/T = 0.25$ and $t/T = 0.75$, respectively. Throughout the rest of the cycle, there exists a disparity in speed between the cylinder and the flow, resulting in an exchange of energy.

In order to confirm this exchange of energy and evaluate the interaction, the vorticity around the flexible cylinder is calculated at two time instants corresponding to: (i) when the velocity between the fluid and cylinder is equal, and (ii) when there is maximum disparity in velocity. The results are depicted in Figure 21, with the left panel labeled "Uniformity" showing the first instant and the second panel labeled "Maximum disparity" showing the second instant.
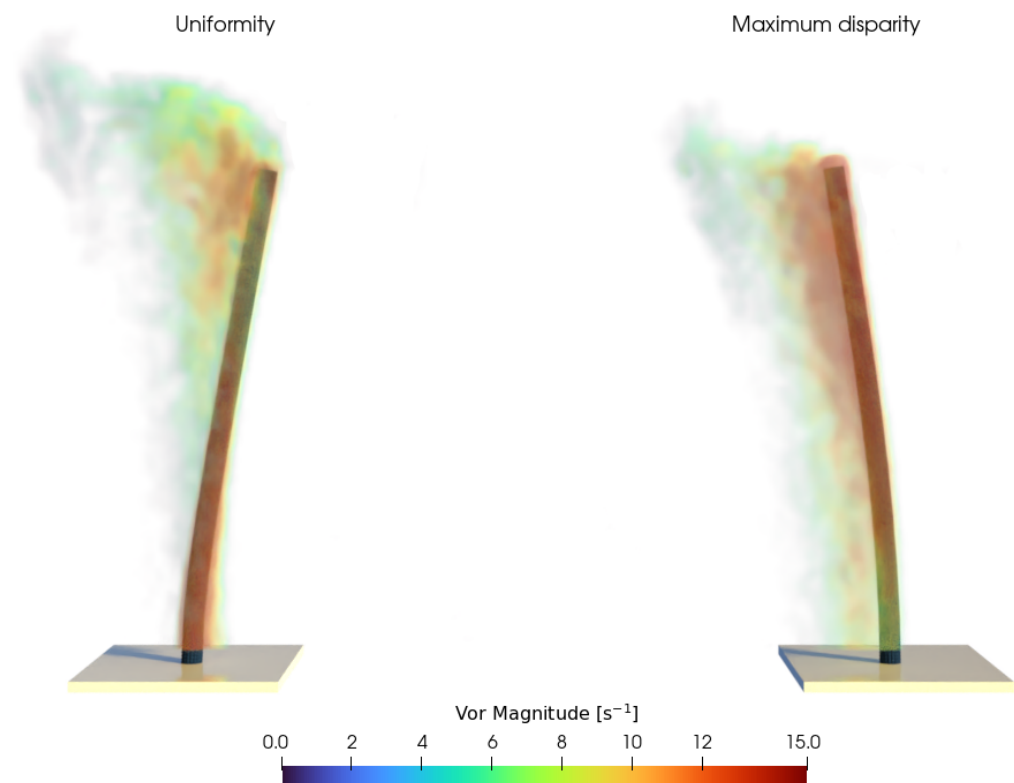

Figure 21. Visualization of vorticity around the flexible cylinder at two distinct time instants, highlighting contrasting postures. The first, labeled 'Uniformity', depicts equal flow and cylinder velocities, while the second, termed 'Maximum Disparity', illustrates the greatest disparity between these velocities. Vorticity is computed and volume rendered for each posture.

Vorticity serves as a direct indicator for the presence of turbulence and the formation of vortex structures. The objective of examining the vorticity at these two time instants is to gain a detailed understanding of the relationship between energy dissipation and the relative velocity between the cylinder and the fluid.

It is evident that energy dissipation is more significant in the case of maximum disparity, with a more pronounced presence of vorticity, distributed relatively evenly along the length of the cylinder. Conversely, during uniformity, vorticity is predominantly

concentrated along the tip section of the cylinder, indicating the presence of a mixing layer and vortex shedding even when velocities are equal.

Another important observation is the shape of the vorticity plume. In the case of uniformity, the vorticity plume appears to be directed upward. In contrast, in the case of maximum disparity, the vorticity plume is spread in a direction normal to the center line of the cylinder. This is to be expected, given the greater disparity in kinetic energy, which is characterized by a more focused directionality.

In discussing these vorticity plots, two main conclusions are drawn. Firstly, the direct modeling technique employed effectively captures the underlying mechanisms of energy shedding, as represented through vorticity. Secondly, throughout the entire wave cycle, including periods of uniformity, a turbulent wake is present around the cylinder, indicating continuous energy transfer and dissipation. This observation is significant when considering the upper section of a cylinder, as it demonstrates that this section interacts with the fluid throughout the entire cycle, contrary to the often assumed passive behavior.

6.2. Framework Interoperability

The fundamental aim of the proposed framework is to establish a protocol for applying coupled fluid-structure models to address wave–vegetation interaction. The sequence of tests within the framework is summarized in Figure 2 and consists of five elements grouped into three blocks: hydrodynamics, structural dynamics, and coupled wave–vegetation interaction.

Framework interoperability is defined as the generalized applicability for developing wave–vegetation numerical simulations across a variety of combined submodels. In this definition, the submodels consist of two components: the flow solver and the structural solver. Although the present study employs a flow solver based on SPH and a structural solver based on the Euler–Bernoulli beam theory, the framework is theoretically applicable to any other combination of submodels. A selection of examples from the literature is presented and described in accordance with the framework interoperability matrix, as detailed in Table 7.

Table 7. Identification of applications of wave–vegetation coupled models published in the literature along with descriptions of the relevant submodels, including both flow and structural components. Framework interoperability is assessed by identifying applicable blocks for hydrodynamics, structural dynamics, and coupled interactions. Abbreviations: N.A. (Not Applicable), Appl. (Applicable).

	Submodel		Framework Interoperability		
	Flow	**Structural**	**Hydrodynamics**	**Structural Dynamics**	**Coupled Interactions**
Luhar and Nepf [34]	Exp. Velocity	Euler–Bernoulli	N.A.	Appl.	N.A.
Zeller et al. [24]	Exp. Velocity	Euler–Bernoulli	N.A.	Appl.	N.A.
Zhu et al. [63]	NHWAVE	Euler–Bernoulli	Appl.	Appl.	Appl.
Chen et al. [61]	OpenFOAM	Rod theory	Appl.	Appl.	Appl.
Zhu et al. [32]	Exp. Velocity	Mass cable model	N.A.	Appl.	N.A.
Paquier et al. [43]	GPUSPH	Linear spring	Appl.	Appl.	Appl.
Yin et al. [36]	XBeach	Euler–Bernoulli	Appl.	Appl.	Appl.
El Rahi et al. [39]	DualSPHysics	Euler–Bernoulli	Appl.	Appl.	Appl.

One set of models consists of models that only qualify for the structural dynamics tests within the framework. These models (e.g., [32]) use a velocity signal recorded in the laboratory to force a structural model in a one-way coupling fashion without active feedback from the structure to the fluid. Therefore, only the structural dynamics tests of the framework are relevant in this case (excluding the static water tank). A second set of models comprises two-way coupled models, such as [61] or [43], where all five elements of the framework can be tested.

7. Conclusions

The recognition of aquatic vegetation as a critical component in the development of future coastal defense systems highlights the need for innovative numerical tools. These tools are essential to understanding the dynamics of wave–vegetation interactions and subsequent energy exchange. This study introduced a pioneering numerical methodology using the meshfree SPH solver DualSPHysics coupled with the structural solver Chrono to accurately simulate these interactions at the scale of individual stems. Additionally, an experimental dataset focusing on a single flexible cylinder has been presented within this context. The objective of this dataset is to validate the model for swaying motion and force transfer.

A numerical modeling framework has been established and applied to address the coupled interactions between waves and flexible vegetation. Moreover, the interoperability of this framework was demonstrated by an examination of coupled models published in the literature and an evaluation of the framework's applicability. The objective is to establish a standardized protocol that could potentially inform future research. This framework functions solely as a benchmark, and subsequent applications are expected to enhance it by incorporating new elements, such as additional tests or analytical solutions.

With regard to the coupled interactions and results, the numerical model effectively addressed the wave–vegetation interaction problem across the three resolutions presented. The validation was achieved by comparing hydrodynamics, swaying, and force transfer between the numerical model and experiments. The findings indicated that the flexible cylinder experienced a force component induced by the periodic waves, surpassing the restoring forces inherent in the system (stiffness and buoyancy), resulting in a swaying motion. Analysis of the force signal and swaying pattern revealed a single dominant component with a frequency matching that of the forcing environment. Consequently, the cylinder swayed under the first mode without exhibiting any resonance phenomena.

When projecting the results onto the wave–vegetation interaction problem and considering implications for energy dissipation, attention was given to examining the relative velocity between the flexible cylinder and the surrounding flow environment. The results demonstrated a discrepancy in velocity throughout the majority of the wave cycle, with uniformity in velocity between the cylinder and the flow occurring only at two distinct time intervals. This observation was reinforced by an analysis of the vorticity surrounding the flexible cylinder, which demonstrated the capacity of the coupled model to directly resolve energy transfer. Furthermore, it was demonstrated that throughout the wave cycle, irrespective of the relative velocity, distinct patterns of vortex shedding persist within the system. The following observations were made: (1) it is evident that energy dissipation is more significant in the case of maximum disparity, with a more pronounced presence of vorticity, distributed relatively evenly along the length of the cylinder; (2) in contrast, during uniformity, vorticity is predominantly concentrated along the tip section of the cylinder, indicating the presence of a mixing layer and vortex shedding even when velocities are equal.

In conclusion, this study marks the pioneering application of the SPH method to directly resolve coupled interactions. The convergence observed in results between low and high resolutions holds significant importance, as it provides a foundation for future simulations that can bypass the need for computationally demanding high resolutions to capture direct energy transfer. The next critical step is to utilize the same numerical model to simulate an array of multiple flexible cylinders, ideally numbering around three or four. As ongoing advancements in SPH continue, such as variable resolution or multi-GPU implementation [64], addressing wave–vegetation interactions at the meadow scale will become increasingly feasible.

Conflicts of Interest: The authors declare no conflicts of interest.

Abbreviations

The following abbreviations are used in this manuscript:

B	Buoyancy parameter
Ca	Cauchy number
CFD	Computational Fluid Dynamics
D	Cylinder diameter
DDT	Density Diffusion Term
dp	Initial inter-particle distance
E	Young's modulus of Elasticity
F_b	Net buoyancy force
FEA	Finite Element Analysis
FSI	Fluid–Structure Interaction
F_x	Horizontal force component
F_{xmax}	Maximum horizontal force
F_{xmin}	Minimum horizontal force
H	Wave height
h	Water depth
I	Moment of inertia
GPU	Graphics Processing Unit
L	Cylinder length
λ	Wavelength
L_e	Ratio of vegetation length to wave excursion
N	Number of structural segments
NS	Navier–Stokes
Re	Reynolds number
SPH	Smoothed Particle Hydrodynamics
t	Time instant
T	Wave period
U_{norm}	Normalized relative velocity between the fluid and the cylinder
$\bar{X}$	Range of swaying
X_{max}	Maximum horizontal displacement
X_{min}	Minimum horizontal displacement

References

1. Austin, Å.N.; Hansen, J.; Donadi, S.; Bergström, U.; Eriksson, B.; Sundblad, G.; Eklöf, J. Synergistic Effects of Rooted Aquatic Vegetation and Drift Wrack on Ecosystem Multifunctionality. *Ecosystems* **2021**, *24*, 1670–1686. [CrossRef]
2. van Zelst, V.T.M.; Dijkstra, J.T.; van Wesenbeeck, B.K.; Eilander, D.; Morris, E.P.; Winsemius, H.C.; Ward, P.J.; de Vries, M.B. Cutting the costs of coastal protection by integrating vegetation in flood defences. *Nat. Commun.* **2021**, *12*, 6533. [CrossRef]

3.   Zhou, K.; Kong, F.; Yin, H.; Destouni, G.; Meadows, M.E.; Andersson, E.; Chen, L.; Chen, B.; Li, Z.; Su, J. Urban flood risk management needs nature-based solutions: A coupled social-ecological system perspective. *Npj Urban Sustain.* **2024**, *4*, 25. [CrossRef]

4.   Stratigaki, V.; Manca, E.; Prinos, P.; Losada, I.J.; Lara, J.L.; Sclavo, M.; Amos, C.L.; Cáceres, I.; Sánchez-Arcilla, A. Large-scale experiments on wave propagation over Posidonia oceanica. *J. Hydraul. Res.* **2011**, *49*, 31–43. [CrossRef]

5.   Reidenbach, M.A.; Thomas, E.L. Influence of the Seagrass, Zostera marina, on Wave Attenuation and Bed Shear Stress within a Shallow Coastal Bay. *Front. Mar. Sci.* **2018**, *5*, 397. [CrossRef]

6.   Beth Schaefer, R.; Nepf, H. Wave damping by seagrass meadows in combined wave-current conditions. *Limnol. Oceanogr.* **2022**, *67*, 1554–1565. [CrossRef]

7.   Zhang, Y.; Lai, X.; Ma, J.; Zhang, Q.; Yu, R.; Yao, X.; Deng, H. Field study on flow structures within aquatic vegetation under combined currents and small-scale waves. *Hydrol. Process.* **2021**, *35*, e14121. [CrossRef]

8.   Ollivier, Q.R.; Maher, D.T.; Pitfield, C.; Macreadie, P.I. Net Drawdown of Greenhouse Gases (CO_2, CH_4 and N_2O) by a Temperate Australian Seagrass Meadow. *Estuaries Coasts* **2022**, *45*, 2026–2039. [CrossRef]

9.   Borland, H.P.; Gilby, B.L.; Henderson, C.J.; Connolly, R.M.; Gorissen, B.; Ortodossi, N.L.; Rummell, A.J.; Nagelkerken, I.; Pittman, S.J.; Sheaves, M.; et al. Seafloor Terrain Shapes the Three-dimensional Nursery Value of Mangrove and Seagrass Habitats. *Ecosystems* **2023**, *26*, 442–456. [CrossRef]

10.   Raven, J.A.; Osborne, B.A.; Johnston, A.M. Uptake of CO_2 by aquatic vegetation. *Plant Cell Environ.* **1985**, *8*, 417–425. [CrossRef]

11.   Contti Neto, N.; Pomeroy, A.; Lowe, R.; Ghisalberti, M. Seagrass Meadows Reduce Wind-Wave Driven Sediment Resuspension in a Sheltered Environment. *Front. Mar. Sci.* **2022**, *8*, 733542. [CrossRef]

12.   Paquier, A.E.; Meulé, S.; Anthony, E.J.; Larroudé, P.; Bernard, G. Wind-Induced Hydrodynamic Interactions with Aquatic Vegetation in a Fetch-Limited Setting: Implications for Coastal Sedimentation and Protection. *Estuaries Coasts* **2018**, *42*, 688–707. [CrossRef]

13.   Glavovic, B.; Dawson, R.; Chow, W.; Garschagen, M.; Haasnoot, M.; Singh, C. Cross-Chapter 2: Cities and Settlements by the Sea. In *Climate Change 2022: Impacts, Adaptation, and Vulnerability. Contribution of Working Group II to the Sixth Assessment Report of the Intergovernmental Panel on Climate Change*; Pörtner, H.O., Roberts, D.C., Tignor, M., Poloczanska, E.S., Mintenbeck, K., Alegría, A., Craig, M., Langsdorf, S., Löschke, S., Möller, V., et al., Eds.; Cambridge University Press: Cambridge, UK, 2022.

14.   Van Coppenolle, R.; Schwarz, C.; Temmerman, S. Contribution of Mangroves and Salt Marshes to Nature-Based Mitigation of Coastal Flood Risks in Major Deltas of the World. *Estuaries Coasts* **2018**, *41*, 1699–1711. [CrossRef]

15.   Narayan, S.; Beck, M.W.; Reguero, B.G.; Losada, I.J.; Wesenbeeck, B.V.; Pontee, N.; Sanchirico, J.N.; Ingram, J.C.; Lange, G.M.; Burks-Copes, K.A. The effectiveness, costs and coastal protection benefits of natural and nature-based defences. *PLoS ONE* **2016**, *11*, e0154735. [CrossRef]

16.   Booij, N.; Ris, R.C.; Holthuijsen, L.H. A third-generation wave model for coastal regions: 1. Model description and validation. *J. Geophys. Res. Ocean.* **1999**, *104*, 7649–7666. [CrossRef]

17.   Suzuki, T.; Zijlema, M.; Burger, B.; Meijer, M.C.; Narayan, S. Wave dissipation by vegetation with layer schematization in SWAN. *Coast. Eng.* **2012**, *59*, 64–71. [CrossRef]

18.   Nowacki, D.J.; Beudin, A.; Ganju, N.K. Spectral wave dissipation by submerged aquatic vegetation in a back-barrier estuary. *Limnol. Oceanogr.* **2017**, *62*, 736–753. [CrossRef]

19.   Zijlema, M.; Stelling, G.; Smit, P. SWASH: An operational public domain code for simulating wave fields and rapidly varied flows in coastal waters. *Coast. Eng.* **2011**, *58*, 992–1012. [CrossRef]

20.   Cao, H.; Feng, W.; Chen, Y. Numerical Modeling of Wave Transformation and Runup Reduction by Coastal Vegetation of the South China Sea. *J. Coast. Res.* **2016**, *75*, 830–835. [CrossRef]

21.   Marjoribanks, T.I.; Hardy, R.J.; Lane, S.N.; Parsons, D.R. High-resolution numerical modelling of flow—vegetation interactions. *J. Hydraul. Res.* **2014**, *52*, 775–793. [CrossRef]

22.   Wang, M.; Avital, E.J.; Bai, X.; Ji, C.; Xu, D.; Williams, J.J.R.; Munjiza, A. Fluid–structure interaction of flexible submerged vegetation stems and kinetic turbine blades. *Comput. Part. Mech.* **2020**, *7*, 839–848. [CrossRef]

23.   Maza, M.; Lara, J.L.; Losada, I.J. A coupled model of submerged vegetation under oscillatory flow using Navier–Stokes equations. *Coast. Eng.* **2013**, *80*, 16–34. [CrossRef]

24.   Zeller, R.B.; Weitzman, J.S.; Abbett, M.E.; Zarama, F.J.; Fringer, O.B.; Koseff, J.R. Improved parameterization of seagrass blade dynamics and wave attenuation based on numerical and laboratory experiments. *Limnol. Oceanogr.* **2014**, *59*, 251–266. [CrossRef]

25.   Girfoglio, M.; Quaini, A.; Rozza, G. Fluid-structure interaction simulations with a LES filtering approach in solids4Foam. *arXiv* **2021**, arXiv:2102.08011. https://doi.org/10.48550/ARXIV.2102.08011.

26.   Dalrymple, R.A.; Kirby, J.T.; Hwang, P.A. Wave Diffraction Due to Areas of Energy Dissipation. *J. Waterw. Port Coast. Ocean Eng.* **1984**, *110*, 67–79. [CrossRef]

27.   Suzuki, T.; Hu, Z.; Kumada, K.; Phan, L.; Zijlema, M. Non-hydrostatic modeling of drag, inertia and porous effects in wave propagation over dense vegetation fields. *Coast. Eng.* **2019**, *149*, 49–64. [CrossRef]

28.   Augustin, L.N.; Irish, J.L.; Lynett, P. Laboratory and numerical studies of wave damping by emergent and near-emergent wetland vegetation. *Coast. Eng.* **2009**, *56*, 332–340. [CrossRef]

29.   van Veelen, T.J.; Karunarathna, H.; Reeve, D.E. Modelling wave attenuation by quasi-flexible coastal vegetation. *Coast. Eng.* **2021**, *164*, 103820. [CrossRef]

30. Mullarney, J.C.; Henderson, S.M. Wave-forced motion of submerged single-stem vegetation. *J. Geophys. Res. Ocean.* **2010**, *115*, C12061. [CrossRef]

31. Mattis, S.A.; Kees, C.E.; Wei, M.V.; Dimakopoulos, A.; Dawson, C.N. Computational Model for Wave Attenuation by Flexible Vegetation. *J. Waterw. Port Coast. Ocean Eng.* **2019**, *145*, 04018033. [CrossRef]

32. Zhu, L.; Zou, Q.P.; Huguenard, K.; Fredriksson, D.W. Mechanisms for the Asymmetric Motion of Submerged Aquatic Vegetation in Waves: A Consistent-Mass Cable Model. *J. Geophys. Res. Ocean.* **2020**, *125*, e2019JC015517. [CrossRef]

33. Luhar, M.; Nepf, H. Wave-induced dynamics of flexible blades. *J. Fluids Struct.* **2016**, *61*, 20–41. [CrossRef]

34. Luhar, M.; Nepf, H.M. Flow-induced reconfiguration of buoyant and flexible aquatic vegetation. *Limnol. Oceanogr.* **2011**, *56*, 2003–2017. [CrossRef]

35. Morison, J.; Johnson, J.; Schaaf, S. The Force Exerted by Surface Waves on Piles. *J. Pet. Technol.* **1950**, *2*, 149–154. [CrossRef]

36. Yin, K.; Xu, S.; Huang, W.; Liu, S.; Li, M. Numerical investigation of wave attenuation by coupled flexible vegetation dynamic model and XBeach wave model. *Ocean Eng.* **2021**, *235*, 109357. [CrossRef]

37. Roelvink, D.; Reniers, A.; van Dongeren, A.; van Thiel de Vries, J.; McCall, R.; Lescinski, J. Modelling storm impacts on beaches, dunes and barrier islands. *Coast. Eng.* **2009**, *56*, 1133–1152. [CrossRef]

38. Brzenski, J.; Davis, K. Flexible Vegetation And Its Implementation In The Swash Ocean Model. In Proceedings of the OCEANS 2021: San Diego–Porto, San Diego, CA, USA, 20–23 September 2021; pp. 1–6.

39. El Rahi, J.; Martínez-Estévez, I.; Tagliafierro, B.; Domínguez, J.M.; Crespo, A.J.; Stratigaki, V.; Suzuki, T.; Troch, P. Numerical investigation of wave-induced flexible vegetation dynamics in 3D using a coupling between DualSPHysics and the FEA module of Project Chrono. *Ocean Eng.* **2023**, *285*, 115227. [CrossRef]

40. Monaghan, J. Smoothed particle hydrodynamics. *Annu. Rev. Astron. Astrophys.* **1992**, *30*, 543–574. [CrossRef]

41. Domínguez, J.M.; Fourtakas, G.; Altomare, C.; Canelas, R.B.; Tafuni, A.; García-Feal, O.; Martínez-Estévez, I.; Mokos, A.; Vacondio, R.; Crespo, A.J.C.; et al. DualSPHysics: From fluid dynamics to multiphysics problems. *Comput. Part. Mech.* **2022**, *9*, 867–895. [CrossRef]

42. Martínez-Estévez, I.; Tagliafierro, B.; El Rahi, J.; Domínguez, J.; Crespo, A.; Troch, P.; Gómez-Gesteira, M. Coupling an SPH-based solver with an FEA structural solver to simulate free surface flows interacting with flexible structures. *Comput. Methods Appl. Mech. Eng.* **2023**, *410*, 115989. [CrossRef]

43. Paquier, A.E.; Oudart, T.; Le Bouteiller, C.; Meulé, S.; Larroudé, P.; Dalrymple, R.A. 3D numerical simulation of seagrass movement under waves and currents with GPUSPH. *Int. J. Sediment Res.* **2021**, *36*, 711–722. [CrossRef]

44. Tschisgale, S.; Fröhlich, J. An immersed boundary method for the fluid-structure interaction of slender flexible structures in viscous fluid. *J. Comput. Phys.* **2020**, *423*, 109801. [CrossRef]

45. Reis, R.A.; Fortes, C.J.; Rodrigues, J.A.; Hu, Z.; Suzuki, T. Experimental study on drag coefficient of flexible vegetation under non-breaking waves. *Ocean Eng.* **2024**, *296*, 117002. [CrossRef]

46. Tasora, A.; Serban, R.; Mazhar, H.; Pazouki, A.; Melanz, D.; Fleischmann, J.; Taylor, M.; Sugiyama, H.; Negrut, D. Chrono: An Open Source Multi-physics Dynamics Engine. In *High Performance Computing in Science and Engineering*; Lecture Notes in Computer Science; Kozubek, T., Ed.; Springer: Berlin/Heidelberg, Germany, 2016; pp. 19–49.

47. Martínez-Estévez, I.; Domínguez, J.; Tagliafierro, B.; Canelas, R.; García-Feal, O.; Crespo, A.; Gómez-Gesteira, M. Coupling of an SPH-based solver with a multiphysics library. *Comput. Phys. Commun.* **2023**, *283*, 108581. [CrossRef]

48. Wendland, H. Piecewise polynomial, positive definite and compactly supported radial functions of minimal degree. *Adv. Comput. Math.* **1995**, *4*, 389–396. [CrossRef]

49. LO, E.Y.M.; Shao, S. Simulation of near-shore solitary wave mechanics by an incompressible SPH method. *Appl. Ocean Res.* **2002**, *24*, 275–286. [CrossRef]

50. Gotoh, H.; Shibahara, T.; Sakai, T.; Koshizuka, S.; Yabe, T. Sub-particle-scale Turbulence Model for the MPS Method—Lagrangian Flow Model for Hydraulic Engineering. *Adv. Methods Comput. Fluid Dyn. Comput. Fluid Dyn. J.* **2001**, *9*, 339–347.

51. Dalrymple, R.; Rogers, B. Numerical modeling of water waves with the SPH method. *Coast. Eng.* **2006**, *53*, 141–147. [CrossRef]

52. Monaghan, J. Simulating Free Surface Flows with SPH. *J. Comput. Phys.* **1994**, *110*, 399–406. [CrossRef]

53. Batchelor, G.K. *An Introduction to Fluid Dynamics*; Cambridge Mathematical Library, Cambridge University Press: Cambridge, UK, 2000. [CrossRef]

54. Capasso, S.; Tagliafierro, B.; Martínez-Estévez, I.; Domínguez, J.M.; Crespo, A.J.C.; Viccione, G. A DEM approach for simulating flexible beam elements with the Project Chrono core module in DualSPHysics. *Comput. Part. Mech.* **2022**, *9*, 969–985. [CrossRef]

55. Khayyer, A.; Gotoh, H.; Falahaty, H.; Shimizu, Y. An enhanced ISPH–SPH coupled method for simulation of incompressible fluid–elastic structure interactions. *Comput. Phys. Commun.* **2018**, *232*, 139–164. [CrossRef]

56. Monaghan, J. SPH without a Tensile Instability. *J. Comput. Phys.* **2000**, *159*, 290–311. [CrossRef]

57. Turek, S.; Hron, J. Proposal for Numerical Benchmarking of Fluid-Structure Interaction between an Elastic Object and Laminar Incompressible Flow. In *Fluid-Structure Interaction*; Bungartz, H.J., Schäfer, M., Eds.; Springer: Berlin/Heidelberg, Germany, 2006; pp. 371–385.

58. O'Connor, J.; Rogers, B.D. A fluid–structure interaction model for free-surface flows and flexible structures using smoothed particle hydrodynamics on a GPU. *J. Fluids Struct.* **2021**, *104*, 103312. [CrossRef]

59. Williamson, C.H.K. Vortex dynamics in the cylinder wake. *Annu. Rev. Fluid Mech.* **1996**, *28*, 477–539. [CrossRef]

60. Williamson, C.S. Sinusoidal flow relative to circular cylinders. *J. Fluid Mech.* **1985**, *155*, 141–174. [CrossRef]

61. Chen, H.; Zou, Q.P. Eulerian–Lagrangian flow-vegetation interaction model using immersed boundary method and OpenFOAM. *Adv. Water Resour.* **2019**, *126*, 176–192. [CrossRef]
62. Beudin, A.; Kalra, T.S.; Ganju, N.K.; Warner, J.C. Development of a coupled wave-flow-vegetation interaction model. *Comput. Geosci.* **2017**, *100*, 76–86. [CrossRef]
63. Zhu, L.; Chen, Q. Numerical Modeling of Surface Waves over Submerged Flexible Vegetation. *J. Eng. Mech.* **2015**, *141*. [CrossRef]
64. Zhao, Z.X.; Bilotta, G.; Yuan, Q.E.; Gong, Z.X.; Liu, H. Multi-GPU multi-resolution SPH framework towards massive hydrodynamics simulations and its applications in high-speed water entry. *J. Comput. Phys.* **2023**, *490*, 112339. [CrossRef]